Pacific Northwest
NATIONAL LABORATORY

PNNL-33351

Development of a Microwave Quantum Sensing Capability

September 2022

Erik Lentz
Daniel Cain
Christian Boutan

U.S. DEPARTMENT OF ENERGY

Prepared for the U.S. Department of Energy
under Contract DE-AC05-76RL01830

DISCLAIMER

PACIFIC NORTHWEST NATIONAL LABORATORY
operated by
BATTELLE
for the
UNITED STATES DEPARTMENT OF ENERGY
under Contract DE-AC05-76RL01830

Printed in the United States of America

Available to DOE and DOE contractors from the Office of Scientific and Technical Information,
P.O. Box 62, Oak Ridge, TN 37831-0062
www.osti.gov
ph: (865) 576-8401
fax: (865) 576-5728
email: reports@osti.gov

Available to the public from the National Technical Information Service
5301 Shawnee Rd., Alexandria, VA 22312
ph: (800) 553-NTIS (6847)
or (703) 605-6000
email: info@ntis.gov
Online ordering: http://www.ntis.gov

PNNL-33351

Development of a Microwave Quantum Sensing Capability

September 2022

Erik Lentz
Daniel Cain
Christian Boutan

Prepared for
the U.S. Department of Energy
under Contract DE-AC05-76RL01830

Pacific Northwest National Laboratory
Richland, Washington 99354

Acknowledgments

This work is supported by the PNNL Laboratory Directed Research and Development (LDRD) program and in part by the U.S. Department of Energy (DOE), Office of Science, Office of Basic Energy Sciences (BES), Division of Chemical Sciences, Geosciences & Biosciences. It was performed at the Pacific Northwest National Laboratory (PNNL), a facility operated by Battelle for the U.S. Department of Energy, including access to the W.R. Wiley Environmental Molecular Sciences Laboratory (EMSL), a national scientific user facility sponsored by the U.S. DOE Biological and Environmental Research program. Battelle operates PNNL for the U.S. Department of Energy under contract DE-AC05-76RL01830.

Contents

Figures

Tables

No table of figures entries found.

1.0 Introduction

The geopolitical world is at the beginning of a quantum renaissance. Technology has reached a level of sophistication that allows the probing of a new world that operates using a different set of rules marked by quantum entanglement, superposition, and the no-cloning theorem. If we can explore this new world and its counterintuitive rules, we may be able to leverage them to build powerful tools for a wide range of applications, including enhanced encryption, computation, and sensing. Some entities have invested early and heavily in exploring this frontier: China has demonstrated quantum teleportation between a ground station and an orbiting satellite; Google recently met a computational milestone known as quantum supremacy, in which a quantum computer solves a problem that would take a classical computer an infeasible amount of time to solve. While great strides have been made, the early progress has caught many entities off guard. The scope of this project leverages an existing investment in a dilution refrigerator strategically chosen to position Pacific Northwest National Laboratory (PNNL) for a future in low-temperature microwave quantum sensing.

For PNNL to establish a foothold in a quantum sensing research and development (R&D) targeting the MHz–GHz frequency band, new equipment needed to be acquired, new partnerships needed to be formed, and new expertise needed to be acquired through trial and error within the freedom to experiment. Specifically, the goal of this project was to grow three pillars as a foundation for future work in quantum microwave instrumentation.

Tools: Enabling hardware and software that is procured conventionally, custom-built locally, or obtained through a strategic partnership.

Team: Forming a tight-knit, multidisciplinary group of skilled individuals committed to becoming local experts in microwave kinetic (mK) radio frequency (RF) instrumentation.

Ties: Connecting to new quantum information science (QIS) partners that will supply proprietary devices, guide local expertise, and eventually vouch for PNNL as a member of the community.

Finally, a near-term goal, to provide a narrative for laying this three-pillar microwave quantum sensing capability foundation, was needed. Investigating quantum radar as a practical technology was strategically chosen to overlap with PNNL radar expertise, pitched to the PNNL early career open call, and received funding in fiscal year (FY) 2021.

2.0 Strategic Focus: Quantum Radar

Quantum sensing in the microwave band is an emerging area of global R&D that is expected to have significant implications for national security and biomedical applications. Although PNNL is a national leader in classical microwave imaging techniques, before this project, the lab had no experimental capability in this field at the quantum level. Quantum radar is a high-profile example application that seeks to extend the concept of quantum illumination [1] to microwave frequencies and was the strategic focus of this project.

Microwave quantum radar systems are in the early stages of development and testing. Approaches for rendering quantum advantage are also the subject of active research as the practical advantages that may be obtained by such a system are not yet well understood [2]. Specifically, the details of entanglement, entanglement-breaking, and residual correlations must be further researched to evaluate the ability of these systems to improve upon existing classical detection capabilities. This project focused on creating a new experimental capability at PNNL by constructing and characterizing a microwave quantum radar system. It leveraged the significant dilution refrigerator investment and our expertise in microwave imaging radar design. This section presents the details of our approach to developing a quantum radar system and the quantum devices used.

2.1 Theory

RaDaR (Radio Detection and Ranging) is a detection scheme for determining the state of a target system using the return signals from active radio wave transmissions. Repeated observations are used to determine an object's size (reflectivity), location and image (distance and relative angles), and kinematics (velocity from repeated observations and/or Doppler shift). Radar operates through the emission of a radio signal, usually pulsed or otherwise modulated, into open air where it can encounter an object and reflect a portion of that signal back to a receiver, usually placed near the transmitter.

Radars have been proven to be very useful in the limit of high emitted power, high target reflectivity, and high received power compared to backgrounds. Their utility is diminished in the limits of low emitted, reflected, received power, a requirement for non-invasive systems, or systems in the presence of high backgrounds where the system may be overwhelmed by interference power. Quantum sensing has been proposed as a solution to these limitations by using a strictly quantum phenomenon known as entanglement as a means to differentiate signal from background.

Quantum entanglement between objects occurs when the description of that system in Hilbert space contains a component inseparable to the states of the individual bodies. The degree of this inseparability, and across what properties it can occur, varies from system to system. For this project, the relevant entangled properties were the energy and phase of photon pairs created through a nonlinear parametric resonance in superconducting devices known as JPAs (Josephson parametric amplifiers) and JPCs (Josephson parametric converters), as shown in Figure 1. The pairs of entangled signals are generated at cryogenic temperatures within a dilution refrigerator system, with one photon transmitted through a room-temperature environment to encounter target objects before being scattered back to the receiver. It has been recently demonstrated, also using JPAs and JPCs, that this signal can be correlated with the original to obtain performance beyond the capabilities of an equivalent classical radar system, even when entanglement was degraded or lost through observation [3,4,5].

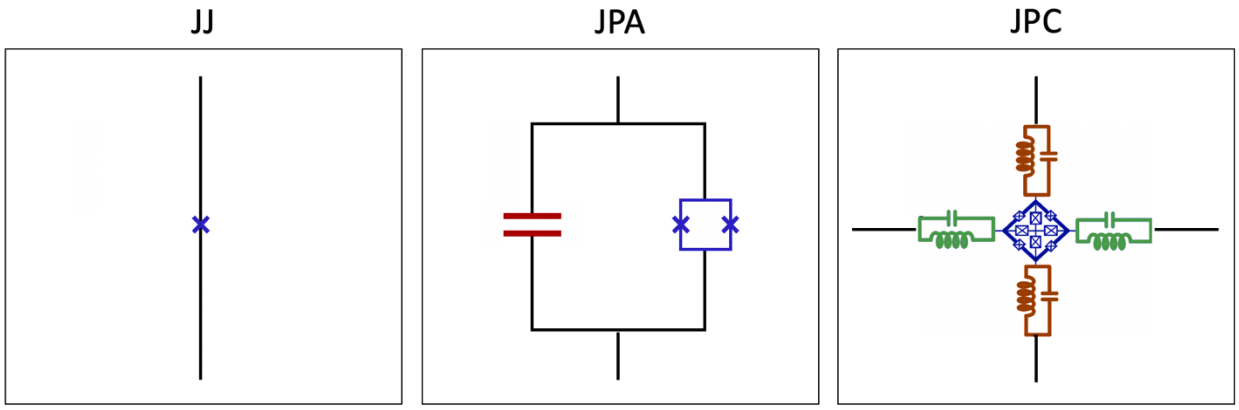

Figure 1. Josephson junction (JJ), JPA, and JPC circuit schematic diagrams.

The nonlinear devices used to facilitate squeezing in this project all have the JJ circuit element in common. Simply put, a JJ element is a weak break in a transmission line, indicated by the "X" in the circuit diagram (Figure 1), made to facilitate quantum tunneling while the line is superconducting and operating at low power. To see how this device can be used to create entangled photons for a quantum radar, consider a superconducting transmission line with (Ginzburg-Landau) complex order parameter ψ. The order parameter may be written in terms of a density and phase so long as the density is nonzero.

$$\psi = \sqrt{n}e^{i\phi},$$

where φ and n are both real fields that can be written as

$$n = \psi^*\psi,$$
$$\phi = Arg(\psi) = Arctan\left(\frac{\psi - \psi^*}{i(\psi + \psi^*)}\right).$$

The order parameter exists on both sides of the JJ, and we will now solve for the dynamics across the junction. The equation of motion for the order parameter is given by a Schrödinger equation

$$i\hbar\partial_t\psi = \frac{-\nabla^2}{2\hbar^2 m}\psi + V_T\psi$$

where V_T is the total potential function of interaction of the order parameter with itself and its environment. The JJ can be considered as two boundaries (A and B) on either side of the junction. The Schrödinger equation boundary equations then become, after assuming no transverse dynamics (relative to the direction of the line)

$$i\hbar\partial_t\psi_A(x_\perp, t) = eV\psi_A + K\psi_B,$$
$$i\hbar\partial_t\psi_B(x_\perp, t) = K\psi_A + eV\psi_B$$

where V is the electric potential difference across the junction, the electric charge of an order parameter quanta is 2e (Cooper pair), and K is the characteristic interaction energy across the

junction. We assume all other contributions to V_T are continuous over the junction.Solving for the phase difference $\varphi = \varphi_B - \varphi_A$, the density tunneling is found by distributing the time derivative over the order parameters and then refactoring terms. After some algebra, one can find the equation of motion for the density flux through boundary A, which equals negative the density flux through boundary B if there is no current leakage

$$\dot{n}_A = \frac{2K\sqrt{n_a n_B}}{\hbar} Sin\left(\varphi(t)\right),$$

and the phases and their difference are found to be

$$\dot{\phi}_A = -\frac{1}{\hbar}\left(eV + K\sqrt{n_B/n_A}Cos\varphi\right),$$
$$\dot{\phi}_B = \frac{1}{\hbar}\left(eV - K\sqrt{n_A/n_B}Cos\varphi\right),$$
$$\dot{\varphi} = \frac{2eV}{\hbar}$$

Note that the voltage across the junction can also vary with time. The density flux is proportional to the current across the JJ, with the coefficient giving a critical current. The coefficient to the phase difference equation of motion divided by 2π is often referred to as the Josephson constant, and is the inverse of the magnetic flux quantum

$$K_J = \frac{1}{\Phi_0} = \frac{1}{2\pi}\frac{2e}{h},$$

where we also name the reduced flux quanta $\varphi_0 = \Phi_0 /2\pi$. π

The JJ element has inductor-like qualities, in that the voltage drop can be expressed with a current derivative

$$V = \frac{\varphi_0}{I_c Cos\varphi}\partial_t I,$$

making the (kinetic) inductance

$$L(I) = \frac{\varphi_0}{I_c Cos\varphi} = \frac{\varphi_0}{\sqrt{I_c^2 - I^2}}$$

There are several effects that can be teased out of these equations, including the DC Josephson effect (direct current across the junction due to tunneling), the AC Josephson effect (alternating current across the junction when given a constant bias voltage V), and the inverse AC Josephson effect (incident radiation at frequency f induced constant voltage bias across junction). Our concern is not with any one of these effects, but a combination of them. To capture the entire set of phenomena of a Josephson junction, we find its Hamiltonian.

Given the Josephson relations

$$I(t) = I_c Sin\varphi,$$
$$\partial_t \varphi = \frac{V(t)}{\varphi_0},$$

where φ_0 is the reduced flux quantum. For small phases, the JJ current and phase map directly onto one another

$$I = I_c \varphi + O(\varphi^2).$$

Solving for the voltage gives a Faraday-analogous relation with the flux phase

$$V = \partial_t \Phi.$$

To find the energy state, consider the fluctuations in energy across the junction (assuming an infinitesimally thin gap) as given by the integral of power flux across the junction

$$\Delta E = \int_{t_1}^{t_2} dt I(t) V(t) = \int_{\Phi_1}^{\Phi_2} d\Phi I$$
$$= \int_{\Phi_1}^{\Phi_2} d\varphi \frac{\Phi_0 I_c Sin\varphi}{2\pi} = -\frac{\Phi_0 I_c}{2\pi} \left(Cos\varphi_2 - Cos\varphi_1\right),$$

and depends only on the end states of the junction, not the path (nonheuristic). The energy is therefore a state function that can be expressed as

$$E(\varphi) = -\frac{\Phi_0 I_c}{2\pi} Cos\varphi = -E_J Cos\varphi,$$

where E_J is named the Josephson energy. To find the Hamiltonian of the JJ, we insert the operators of the degrees of freedom of the superconducting line, the transmon (phonon) fluctuations of the superconductor's order parameter ψ. This only makes sense when the dynamics are in place. As the device will be operated in the RF limit of the circuit, where current wavelength is much larger than the size of the device, we will use a circuit element picture to describe the macroscopic dynamics of the junction.

The minimal addition is to add a capacitor in parallel to the JJ schematic in Figure 1, giving the transmon excitations some mass, which is consistent with the design of the transmon qubit in [6, 7]. The energy of the whole element is then

$$E = \frac{Q^2}{2C} - E_J Cos\varphi,$$

where $C = C_c + C_J$ is the total capacitance, made up of the capacitor and the small JJ capacitance, and Q is the charge on the capacitors. The mode structure of this device is given by an anharmonic oscillator, fitting several modes into the periodic JJ (kinetic) energy, each with their own flux/current wavefunction. The flux decomposed in terms of the modes is

$$\Phi = \sqrt{\frac{\hbar Z}{2}} \sum_{i}^{N_{modes}} C_i \psi^i,$$
$$\hat{\Phi} = \sqrt{\frac{\hbar Z}{2}} \sum_{i}^{N_{modes}} \hat{a}_i \psi^i + \text{ (h.c.)}$$

where the top line is the classical decomposition, and the bottom line is the field operator definition to be used in conjunction with a state vector. The mode creation and annihilation operators $\hat{a}_i^\dagger$, $\hat{a}_i$ are Bose in nature, meaning they commute, supporting multiple occupancy. We are concerned with excitations from the ground state, so our field operator sum will start by only going as high as i= 1. Taking only the first excitation mode, the phase and charge operators become

$$\hat{\Phi} = \sqrt{\frac{\hbar Z}{2}} \left(\hat{a} + \hat{a}^\dagger\right),$$
$$\hat{Q} = \sqrt{\frac{\hbar}{2Z}} \frac{\left(\hat{a} - \hat{a}^\dagger\right)}{i},$$

where Z = L/C is the impedance characteristic of the system. The Hamiltonian operator will then be taken as the energy equation with the phase and charge operators inserted

$$\hat{H} = \frac{\hat{Q}^2}{2C} - E_J Cos\left(\frac{\hat{\Phi}}{\varphi_0}\right).$$

The full Hamiltonian of an aperiodic oscillator is more than we want to track, particularly in the low power ($\varphi << 1$) limit, so we will expand the Hamiltonian about the trivial case and consider only the next-to-lowest-order terms

$$\hat{H} = \frac{\hat{Q}^2}{2C} - E_J \left(1 - \frac{1}{2}\left(\frac{\hat{\Phi}}{\varphi_0}\right)^2 + \frac{1}{24}\left(\frac{\hat{\Phi}}{\varphi_0}\right)^4\right) + O\left(\left(\frac{\hat{\Phi}}{\varphi_0}\right)^6\right),$$

which in terms of the creation/annihilation operators becomes

$$\hat{H}_{trunc} = \omega_a \left(\hat{a}^\dagger \hat{a} + \frac{1}{2}\right) - \frac{I_c \hbar^2 Z^2}{2^2 \times 24 \varphi_0^3} \left(\hat{a} + \hat{a}^\dagger\right)^4,$$

where Z = L/C is the impedance characteristic of the system, and the bare mode frequency is $\omega_a = 1/\sqrt{LC}$.

Each of the quartic terms contributes differently to the system, with some terms creating ($\hat{a}^\dagger\hat{a}^\dagger\hat{a}^\dagger\hat{a}^\dagger$, $\hat{a}^\dagger\hat{a}^\dagger\hat{a}^\dagger\hat{a}$) or destroying ($\hat{a}\hat{a}\hat{a}\hat{a}$, $\hat{a}\hat{a}\hat{a}\hat{a}^\dagger$) excitations, and one term—up to trivial permutation—preserving the number operator of the non-interacting Hamiltonian ($\hat{a}^\dagger\hat{a}\hat{a}^\dagger\hat{a} = N^2$). The excitation number nonpreserving terms will require interactions between states with two or four more/less excitations, depending. The eigenstates that use these terms have energies

separated from the excitation-preserving state on the order of two to four times a bare excitation energy ω_a and the interaction energy

$$E_I = -\frac{I_c \hbar^2 Z^2}{2^2 \times 24 \varphi_0^3},$$

which in the weak interaction limit would be subdominant to the bare energy. Such broad energy differences will be viewed as quickly oscillating about the narrow resonance that will be constructed at the number-preserving state(s); therefore, they can be ignored over times longer than the inverse frequency (using the rotating wave approximation) and the Hamiltonian becomes

$$\hat{H}_{ah} = \omega_a \left(\hat{a}^\dagger \hat{a} + \frac{1}{2} \right) - \frac{I_c \hbar^2 Z^2}{16 \varphi_0^3} \hat{a}^\dagger \hat{a} \hat{a}^\dagger \hat{a}.$$

The form of the an-harmonicity (nonlinearity) is known as a self-Kerr term, with a Kerr coefficient given by

$$\chi = \frac{I_c \hbar^2 Z^2}{16 \varphi_0^3}.$$

The Hamiltonian eigenstates are still those with integer excitations, though their energy levels have now been shifted and are no longer equally spaced, decreasing in spacing by χ(2 N + 1). The nonlinearity of the JJ circuit element will be the primary mechanism by which entangled excitations will be made for the quantum radar system. The next paragraphs will demonstrate in what ways entangled excitations are made in a Josephson parametric circuit, following the Hamiltonian engineering formalism of [6],[7],[8],[9].

To entangle multiple modes, which is what we want for quantum radar, we must first create a circuit with multiple modes that can be mixed. For two-mode squeezing, we will mix three modes together, with the third providing a standard against which the entangled pair will be squeezed. Consider the Hamiltonian of a three-mode system with self-couplings of fourth order and intermode couplings of third order

$$\hat{H}_3 = \omega_a \hat{a}^\dagger \hat{a} + \omega_b \hat{b}^\dagger \hat{b} + \omega_c \hat{c}^\dagger \hat{c} - \frac{E_a}{12} \left(\hat{a} + \hat{a}^\dagger \right)^4 - \frac{E_b}{12} \left(\hat{b} + \hat{b}^\dagger \right)^4 - \frac{E_c}{12} \left(\hat{c} + \hat{c}^\dagger \right)^4 + g_{abc} \left(\hat{a} + \hat{a}^\dagger \right) \left(\hat{b} + \hat{b}^\dagger \right) \left(\hat{c} + \hat{c}^\dagger \right)$$

where E_i is the energy of the i-th JJ, ω_i is the bare energy of mode i, and

$$g_{abc} = \sqrt{\frac{Z_a}{2}} \sqrt{\frac{Z_b}{2}} \sqrt{\frac{Z_c}{2}} g_3$$

is the three-mode coupling strength. The rotating wave approximation (RWA) is more difficult to implement in this case without destroying the three-mode interaction (the exception is when a combination of the mode frequencies +/- ω_a, +/- ω_b, and +/- ω_c come to zero). To circumvent this, one ‘mode’ circuit) may be pumped at a frequency far from its resonance and become stiff (effectively nondynamical with respect to the other modes of the system), and the operator can be replaced by its classical average

$$\hat{c} \rightarrow \langle c \rangle e^{-i(\omega_p t + \phi_p)},$$
$$\hat{c}^\dagger \rightarrow \langle c \rangle e^{i(\omega_p t + \phi_p)}.$$

sending the interaction Hamiltonian to

$$H_{int} \rightarrow g_{abc} \left(\hat{a} + \hat{a}^\dagger\right) \left(\hat{b} + \hat{b}^\dagger\right) \langle c \rangle 2Cos\left(\omega_p t + \phi_p\right)$$

The pump frequency can be chosen to be $\omega_p = |\omega_a \pm \omega_b|$ to produce a gain or conversion process respectively. The interaction Hamiltonian in each of these cases can further be reduced under the RWA (at the pump rate) to

$$\hat{H}_{gain} = g_{abc} \langle c \rangle \left(\hat{a}\hat{b}e^{i\phi_p} + \hat{a}^\dagger \hat{b}^\dagger e^{-i\phi_p}\right),$$
$$\hat{H}_{conv} = g_{abc} \langle c \rangle \left(\hat{a}\hat{b}^\dagger e^{i\phi_p} + \hat{a}^\dagger \hat{b} e^{i\phi_p}\right)$$

where the two can be chosen based on the pump frequency.

Note that one should remain aware of higher order terms as they may interfere in the presence of a driven pump (example: 5th order term g_{abccc} still produces two photons in the a and b modes, effectively altered the coupling strength). Another caution is the contribution from dispersive terms as there are large numbers of pump photons present in the system. Other high order mixing terms containing a number operator of the pump mode $\langle c \rangle^2$ will effectively shift lower order terms, such as the bare frequency of the a-mode through

$$g_{aacc}\hat{a}^\dagger \hat{a}\hat{c}^\dagger \hat{c} = g_{aacc} \langle c \rangle^2 \hat{a}^\dagger \hat{a},$$

where the strength of the term is enhanced by the large pump photon flux.

Next we will see how this Hamiltonian can be realized in a Josephson ring modulator (JRM), the central circuit element of the JPC (Figure 1). The basic JRM, as the name implies, is comprised of a loop containing identical JJs arranged into SQUID loops (the X-ed boxes in the JPC panel), with two half-wavelength resonators around it. Each bare mode is capacitively coupled to a port. Note that the JPC schematic also shows shunting lines through the center of the JRM as a safety feature, which we will omit in the model presented below.

The modes of the ring itself include two polarization modes (a,b) with high and low potential regions at opposite ends of the ring, and a higher frequency mode (c) with high and low potentials alternating on the transmission line between each SQUID loop pair. An illustration of the mode phases is given in Figure 2.

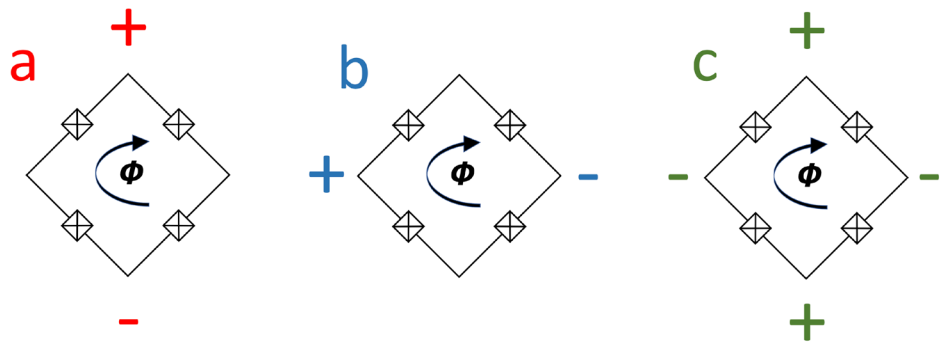

Figure 2. JRM mode diagram.

The Hamiltonian of the JRM without the shunting lines is given by

$$H_{JRM} = -E_J Cos\varphi_1 - E_J Cos\varphi_2 - E_J Cos\varphi_3 - E_J Cos\varphi_4,$$

where φ_i is the phase difference over the i-th JJ. Note that, due to the periodicity of the ring and the low frequency of the JRM compared to the mode wavelengths, the phase differences are set by the external flux

$$\varphi_1 + \varphi_2 + \varphi_3 + \varphi_4 = \varphi_{ext}$$

and are periodic over 2π in the absence of external flux. The modes described in the previous paragraph can be expressed in terms of these phase differences

$$\varphi_a = \varphi_1 - \varphi_2 + \varphi_4 - \varphi_3,$$
$$\varphi_b = \varphi_4 - \varphi_1 + \varphi_3 - \varphi_2,$$
$$\varphi_c = \varphi_1 - \varphi_2 - \varphi_4 + \varphi_3.$$

We may convert the Hamiltonian in terms of the local phase differences to one in terms of the mode phase differences. After some algebra, the JRM Hamiltonian may be written as

$$H_{JRM} = -4E_J Cos\frac{\varphi_a}{2} Cos\frac{\varphi_b}{2} Cos\varphi_c Cos\frac{\varphi_{ext}}{4} - 4E_J Sin\frac{\varphi_a}{2} Sin\frac{\varphi_b}{2} Sin\varphi_c Sin\frac{\varphi_{ext}}{4},$$

where again φ_{ext} is the total flux through the JRM. In the limit of small mode fluxes, the Hamiltonian expands to

$$H_{JRM} = E_J Cos\frac{\varphi_{ext}}{4}\left(\frac{\varphi_a^2}{2} + \frac{\varphi_b^2}{2} + 2\varphi_c^2 - 4\right) - E_J Sin\frac{\varphi_{ext}}{4}\varphi_a\varphi_b\varphi_c + O(\varphi^4)$$

which mimics the model interaction Hamiltonian used in the previous paragraphs. The first term contributes to the linear inductance energy of the JRM and can be absorbed into the bare modes, while the second term gives the three-mode coupling.

The JRM can be operated in the two parametric processes covered earlier: (phase-preserving) gain and conversion. In the larger JPC, the macroscopic modes evolve according to the

Langevin equations of motion as they vary slowly and out of resonance with the rest of the system (recall that an assumption of the RWA is that the rest of the system be considered stiff)

$$\frac{d\hat{a}}{dt} = \frac{i}{\hbar}\left[\hat{H}, \hat{a}\right] - \kappa_a/2\hat{a} + \sqrt{\kappa_a}\hat{a}_{in},$$
$$\sqrt{\kappa_a}\hat{a} = \hat{a}_{in} + \hat{a}_{out},$$

where κ_a is the bandwidth of the mode, and the "in" and "out" operators represent the incoming and outgoing waves to the JPC matched at the boundary to the internal mode a. The b and c modes have their own governing equations. Using the gain Hamiltonian, the a and b mode Langevin equations become

$$\frac{d\hat{a}}{dt} = -i\omega_a\hat{a} - ig_{abc}\hat{b}^\dagger \langle c\rangle e^{i\phi_p} - \kappa_a/2\hat{a} + \sqrt{\kappa_a}\hat{a}_{in},$$
$$\frac{d\hat{b}}{dt} = i\omega_b\hat{b} - ig_{abc}\hat{a}^\dagger \langle c\rangle e^{i\phi_p} - \kappa_b/2\hat{b} + \sqrt{\kappa_b}\hat{b}_{in},$$

implying two closed systems of equations between â and $b^\dagger$, and b and $â^\dagger$. To find the transmission/reflection properties of the JPC, we can separate the modes into their incoming and outgoing components, resulting in the equations in frequency space

$$\begin{aligned}
&\left(i\omega_1 - i\omega_a - \kappa_a/2\right)\hat{a}_{out}[\omega_1] - ig_{abc}\langle c\rangle^2\sqrt{\kappa_a/\kappa_b}e^{-i\phi_p}\hat{b}^\dagger_{out}[-\omega_2] \\
&= \left(i\omega_a - i\omega_1 - \kappa_a/2\right)\hat{a}_{in}[\omega_1] + ig_{abc}\langle c\rangle^2\sqrt{\kappa_a/\kappa_b}e^{-i\phi_p}\hat{b}^\dagger_{in}[-\omega_2], \\
&\left(-i\omega_2 + i\omega_b - \kappa_b/2\right)\hat{b}^\dagger_{out}[-\omega_2] + ig_{abc}\langle c\rangle^2\sqrt{\kappa_b/\kappa_a}e^{i\phi_p}\hat{a}_{out}[\omega_a] \\
&= \left(-i\omega_b + i\omega_2 - \kappa_b/2\right)\hat{b}^\dagger_{in}[-\omega_2] - ig_{abc}\langle c\rangle^2\sqrt{\kappa_b/\kappa_a}e^{i\phi_p}\hat{a}_{in}[\omega_1],
\end{aligned}$$

These linear equations can be organized into a scattering (or transmission) matrix form

$$\begin{bmatrix}\hat{a}_{out}[\omega_1] \\ \hat{b}^\dagger_{out}[-\omega_2]\end{bmatrix} = \begin{bmatrix}S_{11} & S_{21}e^{-i\phi_p} \\ S^*_{21}e^{i\phi_p} & S_{22}\end{bmatrix}\begin{bmatrix}\hat{a}_{in}[\omega_1] \\ \hat{b}^\dagger_{in}[-\omega_2]\end{bmatrix}$$

where the matrix components expand to

$$S_{11} = \frac{ig_{abc}\langle c\rangle^2\sqrt{\kappa_b/\kappa_a}e^{i\phi_p} \times (i\omega_a - i\omega_1 - \kappa_a/2) - ig_{abc}\langle c\rangle^2\sqrt{\kappa_b/\kappa_a}e^{i\phi_p} \times (i\omega_1 - i\omega_a - \kappa_a/2)}{(i\omega_1 - i\omega_a - \kappa_a/2) \times ig_{abc}\langle c\rangle^2\sqrt{\kappa_b/\kappa_a}e^{i\phi_p}},$$

$$S_{22} = \frac{ig_{abc}\langle c\rangle^2\sqrt{\kappa_a/\kappa_b}e^{-i\phi_p} \times (-i\omega_2 + i\omega_b - \kappa_b/2) - ig_{abc}\langle c\rangle^2\sqrt{\kappa_a/\kappa_b}e^{-i\phi_p} \times (-i\omega_b + i\omega_2 - \kappa_b/2)}{-ig_{abc}\langle c\rangle^2\sqrt{\kappa_a/\kappa_b}e^{-i\phi_p} \times (-i\omega_2 + i\omega_b - \kappa_b/2)},$$

$$S_{21}e^{-i\phi_p} = S^*_{12}e^{-i\phi_p} = \frac{ig_{abc}\langle c\rangle^2\sqrt{\kappa_a/\kappa_b}e^{-i\phi_p} \times ig_{abc}\langle c\rangle^2\sqrt{\kappa_b/\kappa_a}e^{i\phi_p} + (-i\omega_b + i\omega_2 - \kappa_b/2) \times (i\omega_1 - i\omega_a - \kappa_a/2)}{(i\omega_1 - i\omega_a - \kappa_a/2) \times ig_{abc}\langle c\rangle^2\sqrt{\kappa_b/\kappa_a}e^{i\phi_p}}.$$

Analogous results can be found for the b and $â^\dagger$ evolution.

Near resonance ($\omega_a = \omega_1$ and $\omega_b = \omega_2$) the gain structure in the scattering components become very clear, with the same mode gain of

$$G = \frac{1+\rho^2}{1-\rho^2}$$

and a trans-mode gain of

$$G_T = G - 1$$

where the pump parameter is found to be

$$\rho = \frac{g_{abc}\,\langle c \rangle}{\sqrt{\kappa_a \kappa_b}}$$

The trans-channel component also induces a phase difference of $\pi/2 - \varphi_p$ into the outgoing mode. A similar process can be made for the conversion Hamiltonian, but we are more concerned with the creation of pairs of entangled excitations and will focus on the gain configuration here.

To understand the nature of the entanglement that can be induced into the non-pump modes, note that the exponential of the interaction Hamiltonian is of a similar form as a two-mode squeezing operator

$$\hat{S}(z) = exp\left(z^* \hat{a}\hat{b} - z\hat{a}^\dagger \hat{b}^\dagger\right),$$

where z is a complex number used to parameterize the degree and phase information of the squeezing. This computation applied to the mode creation and annihilation operators is straightforward if one uses the following identity between arbitrary operators

$$e^{\hat{A}}\hat{B}e^{-\hat{A}} = \sum_{k=0}^{\infty} \frac{1}{k!}\left[\hat{A}, \left[\hat{A}, ..., [\hat{A}, \hat{B}]...\right]\right]$$

where the k-th term in the sum has k commutation relations. The skew squeeze kernel operator is Hermitian, implying that its exponentiation is also Hermitian, and its conjugate translates to flipping the kernel operator's sign. The commutators of the kernel operator and the mode creation and annihilation operators are

$$[z^*\hat{a}\hat{b} - z\hat{a}^\dagger\hat{b}^\dagger, \hat{a}] = -z[\hat{a}^\dagger\hat{b}^\dagger, \hat{a}] = z\hat{b}^\dagger,$$
$$[z^*\hat{a}\hat{b} - z\hat{a}^\dagger\hat{b}^\dagger, \hat{a}^\dagger] = +z[\hat{a}\hat{b}, \hat{a}^\dagger] = z\hat{b}.$$

Enumerating over n nested commutators operating on an annihilation operator gives

$$\left[\hat{A}, \left[\hat{A}, ..., [\hat{A}, \hat{a}]...\right]\right] = |z|^n \hat{b} \text{ (n even)},$$
$$- z|z|^{n-1}\hat{b}^\dagger \text{(n odd)},$$

with analogous results for the creation operator. The action on the a-mode creation and annihilation operators therefore is

$$\hat{S}^\dagger \hat{a} \hat{S} = \hat{b} \sum_{k=0}^{\infty} \frac{|z|^{2k}}{(2k)!} - \hat{b}^\dagger \frac{z}{|z|} \sum_{k=0}^{\infty} \frac{|z|^{2k+1}}{(2k+1)!},$$
$$\hat{S}^\dagger \hat{a}^\dagger \hat{S} = \hat{b}^\dagger \sum_{k=0}^{\infty} \frac{|z|^{2k}}{(2k)!} - \hat{b} \frac{z}{|z|} \sum_{k=0}^{\infty} \frac{|z|^{2k+1}}{(2k+1)!},$$

which simplifies to

$$\hat{S}^\dagger \hat{a} \hat{S} = cosh(|z|)\hat{b} - e^{i\varphi} sinh(|z|)\hat{b}^\dagger,$$
$$\hat{S}^\dagger \hat{a}^\dagger \hat{S} = -e^{i\varphi} sinh(|z|)\hat{b} + cosh(|z|)\hat{b}^\dagger,$$

with analogous results for the b mode operators. In summary, the two-mode squeezing operator shifts photons in one mode into squeezed photons in the other mode. Recall that the JPC is being operated in the **gain** and not the conversion configuration.

Evolving an operator in time by the Hamiltonian, or by the Langevin equations, is given by the action by the integral operator

$$\hat{U}(t,0) = exp\left(i\hat{H}t/h\right)$$

so long as the Hamiltonian description is sufficient and the Hamiltonian itself is not time dependent. This integral operator can be expressed as a squeezing operator through a simple reparameterization of the pump phase φ_p to φ_p - π/2

$$\begin{aligned}
\hat{U}(t,0) &= exp\left(i\left(\hat{H}_0 + \hat{H}_{gain}\right)t/h\right), \\
&= exp\left(i\left(\hat{H}_0 + g_{abc}\langle c\rangle\left(\hat{a}\hat{b}e^{i\phi_p} + \hat{a}^\dagger\hat{b}^\dagger e^{-i\phi_p}\right)\right)t/h\right), \\
&= exp\left(i\left(\hat{H}_0 + g_{abc}\langle c\rangle\left(\hat{a}\hat{b}(-i)e^{i\varphi_p} + \hat{a}^\dagger\hat{b}^\dagger ie^{-i\varphi_p}\right)\right)t/h\right), \\
&= exp\left(i\left(\hat{H}_0 - ig_{abc}\langle c\rangle\left(\hat{a}\hat{b}e^{i\varphi_p} - \hat{a}^\dagger\hat{b}^\dagger e^{-i\varphi_p}\right)\right)t/h\right), \\
&= exp\left(i\hat{H}_0 t + ln(\hat{S}(z = tg_{abc}\langle c\rangle e^{i\varphi}/h))\right),
\end{aligned}$$

where we note that the bare Hamiltonian H_0 and the gain Hamiltonian H_{gain} (and therefore the squeeze operator) do not commute. The squeezing parameter may be related to the gain and phase shift of the squeezing process

$$|z| = tg_{abc} \langle c \rangle ,$$
$$Arg(z) = \phi_p,$$

where the time dependence on the squeezing parameter modulus appears to increase without bound though the losses of the physical modes of the system limit the squeezing to the gain parameter $|z|_{max} = \cosh^{-1}(G^{1/2})$.

Incoming waves along each non-pumped bare mode will be amplified by the gain and squeezed, but will also be mixed by the three-mode interaction term into the other mode. This was shown above by the skew squeezing operator. The new true modes can be calculated by diagonalizing the Langevin equations. Our primary use case is to keep the inputs to the two degrees of freedom (bare modes a and b, or some other basis) at a thermal or vacuum state, which produce random fluctuations of a known spectrum. These fluctuations are then driven by the pump and amplified. The result from each individual bare mode can be seen from the results of the scatter matrix, though we note that the outputs maintain un-squeezed thermal profiles. The degrees of freedom that demonstrate squeezing are the mixed operators

$$\hat{m}_{\pm} = \frac{1}{2}\left(\hat{a} \pm \hat{b}\right),$$
$$\hat{m}_{\pm}^{\dagger} = \frac{1}{2}\left(\hat{a}^{\dagger} \pm \hat{b}^{\dagger}\right),$$

which are seen to be the true modes of the system. To see the squeezed nature of the modes, let us act on them with the squeezing operator

$$\hat{S}^{\dagger}\hat{m}_{\pm}\hat{S} = cosh(|z|)\hat{m}_{\pm} - e^{i\varphi}sinh(|z|)\hat{m}_{\pm}^{\dagger},$$
$$\hat{S}^{\dagger}\hat{m}_{\pm}^{\dagger}\hat{S} = -e^{i\varphi}sinh(|z|)\hat{m}_{\pm} + cosh(|z|)\hat{m}_{\pm}^{\dagger},$$

The quadrature representation of each mode is given by

$$\hat{I}_{\pm} = \hat{m}_{\pm} + \hat{m}_{\pm}^{\dagger} = \frac{1}{2}\left(\hat{a} \pm \hat{b} + \hat{a}^{\dagger} \pm \hat{b}^{\dagger}\right),$$
$$\hat{Q}_{\pm} = \frac{1}{i}\left(\hat{m}_{\pm} - \hat{m}_{\pm}^{\dagger}\right) = \frac{1}{2i}\left(\hat{a} \pm \hat{b} - \hat{a}^{\dagger} \mp \hat{b}^{\dagger}\right),$$

which when squeezed results in

$$\hat{S}^{\dagger}\hat{I}_{\pm}\hat{S} = \left(cosh(|z|) - e^{i\varphi}sinh(|z|)\right)\hat{I}_{\pm},$$
$$\hat{S}^{\dagger}\hat{Q}_{\pm}\hat{S} = \left(e^{i\varphi}sinh(|z|) + cosh(|z|)\right)\hat{Q}_{\pm},$$

Each of these modes is squeezed/entangled, though each with its own phase. Note that the labeling of the squeezed modes' quadrature operator differs from much of the rest of the literature by a sign. Before discussing the layout of the quantum radar system, let us touch on the impact of magnetic fields on the JPC.

The presence of AC and DC external magnetic sources will be canceled in the superconducting lines by compensating currents. These currents may impact the Josephson inductance, as we will see. Many JJ-based quantum amplifiers and converters use magnetic flux as a bias (DC) or pumping (AC) mechanism to tune the properties of the device.

The presence of a DC magnetic field producing a flux through the JRM will alter the Faraday-like equation to contain an actual magnetic flux term

$$V = \partial_t \left(\Phi + \Phi_B \right)$$

where

$$\Phi_B = \iint_{JRM} \vec{B} \cdot \vec{n} dA$$

is the flux of the magnetic field through the JRM. Assuming the magnetic flux is spread evenly over the JRM, the Hamiltonian of the JRM is then updated by the shift in flux

$$\begin{aligned} H_{JRM} \rightarrow & -E_J Cos\left(\varphi_1 + \varphi_B/4\right) - E_J Cos\left(\varphi_2 + \varphi_B/4\right) \\ & - E_J Cos\left(\varphi_3 + \varphi_B/4\right) - E_J Cos\left(\varphi_4 + \varphi_B/4\right), \\ & = -4E_J Cos\frac{\varphi_a}{2} Cos\frac{\varphi_b}{2} Cos\varphi_c Cos\frac{\varphi_{ext} + \varphi_B}{4} - 4E_J Sin\frac{\varphi_a}{2} Sin\frac{\varphi_b}{2} Sin\varphi_c Sin\frac{\varphi_{ext} + \varphi_B}{4}, \\ & = E_J Cos\frac{\varphi_{ext} + \varphi_B}{4}\left(\frac{\varphi_a^2}{2} + \frac{\varphi_b^2}{2} + 2\varphi_c^2 - 4\right) - E_J Sin\frac{\varphi_{ext} + \varphi_B}{4}\varphi_a\varphi_b\varphi_c + O(\varphi^4), \end{aligned}$$

where recall that φ_{ext} is the total flux sans magnetic field. The net magnetic flux does not indepedently shift any of the mode fluxes, instead entering only as an interaction strength coefficient by shifting the total external flux. Note that the strength of the mode kinetics and the strength of the three-mode interaction are out of phase with respect to the magnetic flux by π/2, implying that for DC magnetic fluxes the mode mixing strength will be largest when the mode masses are experiencing their largest tuning rate with respect to change in flux. Another common tuning mechanism is the pump (mode c) voltage amplitude, which increases the interaction strength and shifts locations of the resonance as covered in an earlier subsection.

Next we will discuss how thermal fluctuations translate into detectable beams for a quantum radar and the entanglement properties of these beams. The language with which we set up entanglement of transmon pairs has been on an excitation-by-excitation basis, namely that the modes of the respective channel ports (Signal, Idle) mix in the NL system and the new modes are squeezed along their quadrature representation. This corresponds to the S and I channels appearing entangled over their quadratures as the modes are not separable over the channel projection operators.

The output beams from each channel ($\hat{a}_{out}$, b_{out}) still quite weak after exiting the JPC. This is required as we do not want to drive the device too hard as higher non-linear terms will gain

relevance and add further mixing to the system. Therefore, we will require further amplification if we want to emit them into the air, have them reflect off a potential target, and enter into a receiver with sufficient power to be used as a radar. The first stage of amplification for both beams are a HEMT (high electron mobility transistor) amplifier. Amplifiers of this type will increase the power of an incoming signal by a gain of 35-40 dB (and noise power equivalent of approximately 4 Kelvin). However, what is most important to us is the impact to the beams' entanglement properties. An HFET amplifier effectively measures an input beam's state and strengthens it by creating copies of that measured state in a phase preserving manner. The output amplified beam is now describable by a classical field.

Unfortunately, this process destroys the entanglement between the two JPC beams, meaning our quantum radar in fact does not maintain its quantum properties throughout. Fortunately, the act of measuring the entangled excitations does not destroy all correlations of the pair. These residual correlations are to be used in a quantum illumination radar [3, 4, 5]. Quantum illumination radar has the advantage that it does not require preservation of quantum entanglement through use of an extensive storage ring for one of the beams. Instead, beams not passed to a target may be digitized and placed in long-term storage until needed.

There are several measures that can be used to detect once-entangled pairs of excitations. Perhaps the most straightforward is the non-separability measure, which uses the quadratures of a signal to determine if it contains non-classical correlations. The measure, here represented as being performed over the normal modes of the signal and idler channels,

$$\Delta_{\pm} = \langle Q_{\pm}^2 \rangle + \langle I_{\pm}^2 \rangle$$

is less than one only if the modes contain entanglement-based correlations. Otherwise the measure is unity or greater. Note that the expectation values assume that one is integrating over coincidentally emitted excitation pairs as non-coincidentally emitted pairs will obviously be separable. When the target distance is unknown, one can implement a time delay to the expectation integrals, where the actual delay should occupy an optimum.

One can also form a variety of signal-to-noise (SNR) measures. A measure based on the number of excitations received when a target is present compared to not is

$$SNR_{QI/CL} = \frac{(\langle \hat{N}_1 \rangle - \langle \hat{N}_0 \rangle)^2}{2\left(\sqrt{(\Delta N_1)^2} + \sqrt{(\Delta N_0)^2}\right)^2}$$

where (1) indicates the presence of a target and (0) the absence of a target. The number operators are given by

$$\hat{N}_i = \hat{N}_{i,+} - \hat{N}_{i,-}$$

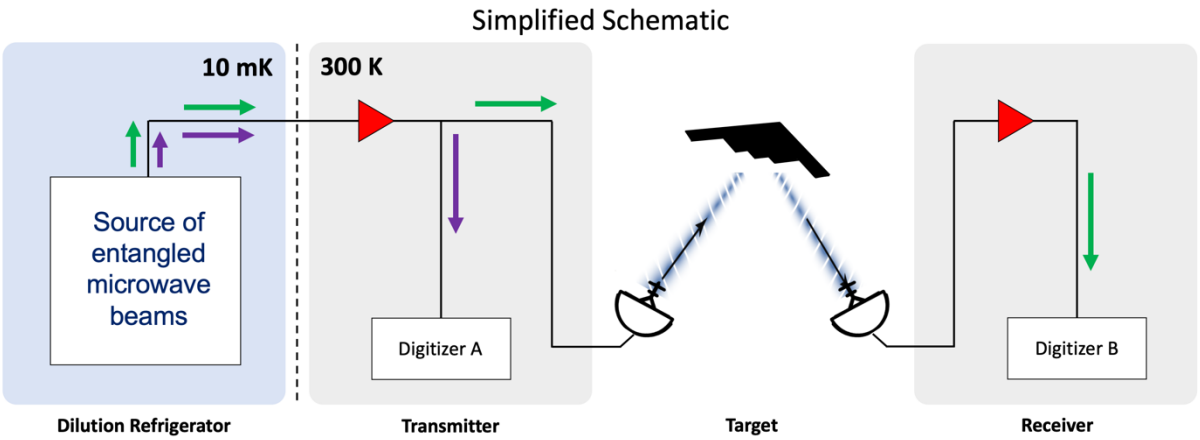

Figure 3. Cartoon of quantum radar schematic

3.0 Building a Capability

The timeline for this two-year project is shown in Table 1. Design specifics were held up by and dependent on what type of 'quantum' non-linear device would be obtainable through collaboration. Long lead-time procurements not tied to device or final design specifics were made in the first quarter.

Microwave Quantum Sensing LDRD Project Timeline									
		FY21				FY22			
Task	Task Description	Q1	Q2	Q3	Q4	Q1	Q2	Q3	Q4
1	Complete agreement with quantum device collaborator								
2	Complete procurement process for components								
3	Test room-temperature components								
4	Develop correlation and analysis software								
5	Build room-temperature receiver/digitizer subsystem								
6	Test room-temperature receiver/digitizer/software								
7	Obtain quantum device from collaborator	Not commercially available							
8	Obtain cryogenic components	Long lead times							
9	Complete quantum device characterization								
10	Test quantum radar system (without target)								
11	Comare classical vs quantum performance (with target)								
12	Perform final tests and analysis								

Table 2. Project planned timeline

3.1 Devices obtained through strategic partnerships.

At the heart of the quantum radar system is a non-linear, parametric device providing a source of entangled photons. In 2021 (and to a large extent even today, at the time of writing), these devices were not commercially available for purchase.

Table 2. List of Potential Collaborators

Institution	Point of Contact	Device
MIT/Lincoln Laboratory	William Oliver, PhD	TWPA
Raytheon BBN Technologies	Andrew Wagner, PhD	JPA
Washington University	Kater Murch, PhD	JPA
University of Chicago	David Schuster, PhD	JPA
University of Pittsburgh	Michael Hatridge, PhD	JPC

The onset of the project began with a networking challenge: convince a future collaborator to donate a quantum device to the project without leverage or monetary incentives. Table 2 contains a list of institutions contacted over a series of virtual meetings in FY21 Q1 and Q2 for possible donation of quantum parametric device to the project. Some contacts became unresponsive while others showed interested in collaboration. MIT/LL was willing to partner if we could support the graduate student needed to oversee the repurposing their TWPA devices for two-mode squeezing. This partnership alone would have cost significantly more than the entire yearly budget for the project. By Q3 of FY21 (1/4 of the way through the two-year project duration), the PI had received donated devices from three collaborators: one JPA from BBN Raytheon through point of contact Andrew Wagner, one JPA from the University of Chicago through point of contact David Schuster, and three JPCs from the University of Pittsburgh through point of contact Michael Hatridge.

Figure 4. Devices received from new partners at BBN Raytheon (Andrew Wagner), University of Chicago (David Schuster), and University of Pittsburgh (Michael Hatridge).

3.2 Design

Given early success that resulted in new collaborators and a variety of obtained devices in hand, there was some freedom in the final design. A design closely following [3] was adopted.

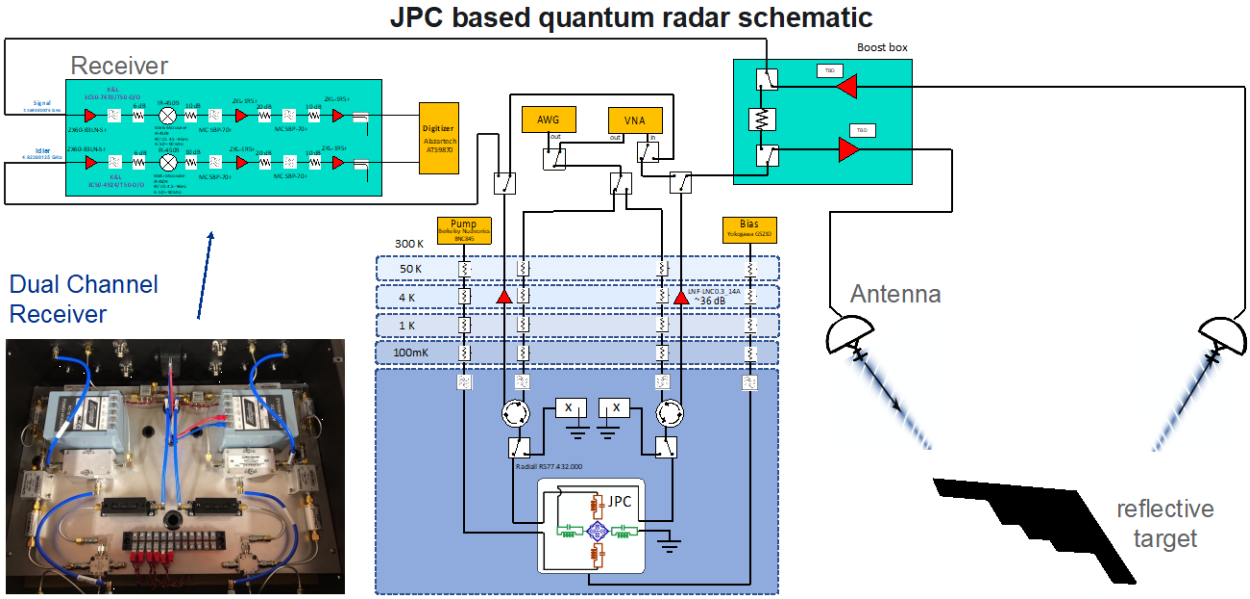

Figure 5. Quantum Radar tabletop experiment schematic

In this scenario, the Signal and Idler ports from a JPC (bottom center of Figure 5) emit pairs of entangled excitations when pumped by a tone with a frequency that is equal to the sum of the Signal and Idler mode frequencies. The JPC is thermally tied to the mixing chamber stage of a dilution refrigerator, anchoring its thermal noise characteristics. Signal and Idler microwave photons then take parallel paths through circulators, up through the various temperature stages of the dilution refrigerator, each receive 35-40 dB of gain at the 4K stage, and exit the fridge. At room temperature, in a custom receiver box, the signals are further amplified, bandpass filtered, mixed down to 70 MHz, and digitized by a two channel AlazarTech ATS9870. In software, correlations between the channels can be explored and used to demonstrate squeezing. If the project plan had proceeded to full maturity, the Signal line path would have been reconfigured to involve transmission from an antenna, reflection off a target, and pickup from another antenna before mix-down and digitization, see right side of Figure 5.

3.3 Test Stand and Cold Hardware

At the start of the project, in parallel with efforts obtain quantum devices, commercially available supporting electronics were procured and assembled.

3.3.1 Cold Hardware

Low Noise Factory LNF-LNC0.3_14A cryogenic HEMT amplifiers providing 35-40 dB over the 0.3-14 GHz band and Low Noise Factory LNF-CIC4_12A cryogenic circulators specified to operate in the 4-12 GHz band were obtained from Quantum Microwave. Custom copper brackets were machined in-house to allow for mounting on the 4K and MXC stages. Magnetic cryoperm shielding was designed to fit PNNL's BlueFors LD400 dilution refrigerator cold space dimensions and ordered through Quantum Plating Solutions (Left panel of Figure 6). Magnetic shielding was the pacing step for successful cryogenic measurements and arrived in November FY 22. Miscellaneous components such as: DC blocks, bandpass filters, attenuators, and cables were obtained from various vendors such as Fairview Microwave, K&L, Mini-Circuits.

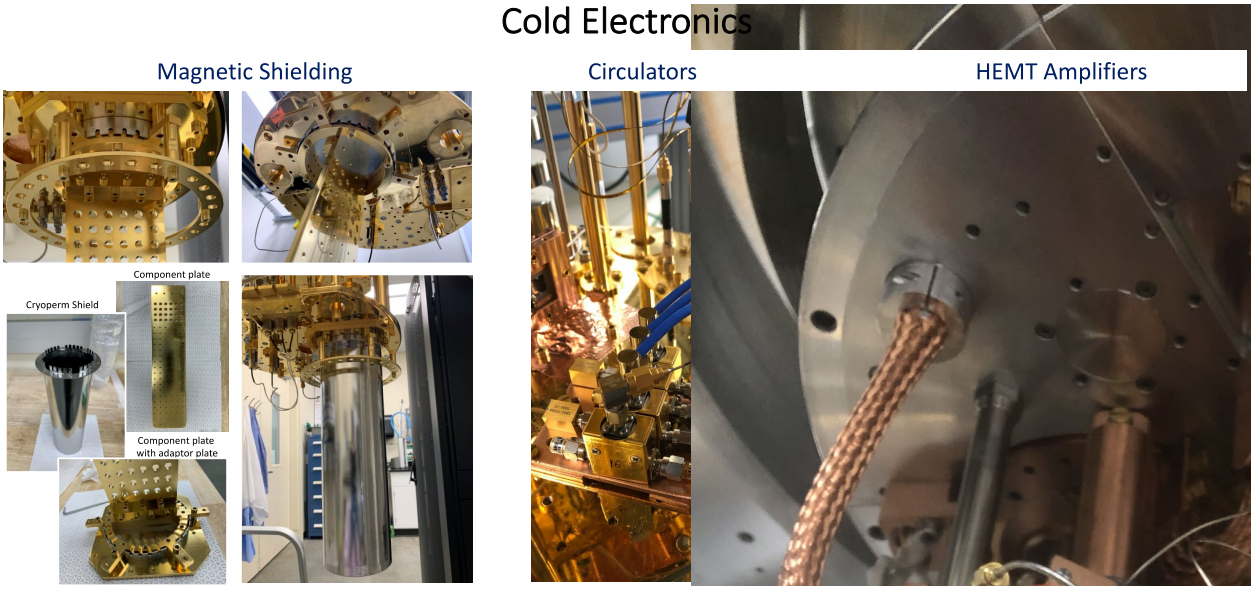

Figure 6. Cryogenic components such as Cryoperm magnetic shielding (left), circulators (center), and HEMT amplifiers (right).

3.3.2 Warm Hardware

A lockable Tripp Lite server rack (Figure 7, right) was procured to house the in-flux of new RF equipment critical to this project: Keysight Vector Network Analyzer (VNA), Dell server housing the 2-channel AlazarTech ATS9870 digitizer, Yokogawa GS210 low noise current source for biasing quantum devices, SignalCore signal generator for pumping quantum noise limited amplifiers, a custom dual-channel heterodyne receiver, a Holzworth HSX9002A local oscillator, two Mini-Circuits RC-8SPDT-A18 switch matrices, and a Low Noise Factory power brick for powering HEMT amplifiers in the refrigerator. A custom feedthrough plate of RF bulkheads was designed to fit on top the rack for cable management and strain relief reasons. All components in the rack were to communicate through the network, allowing for easy automation of data-runs.

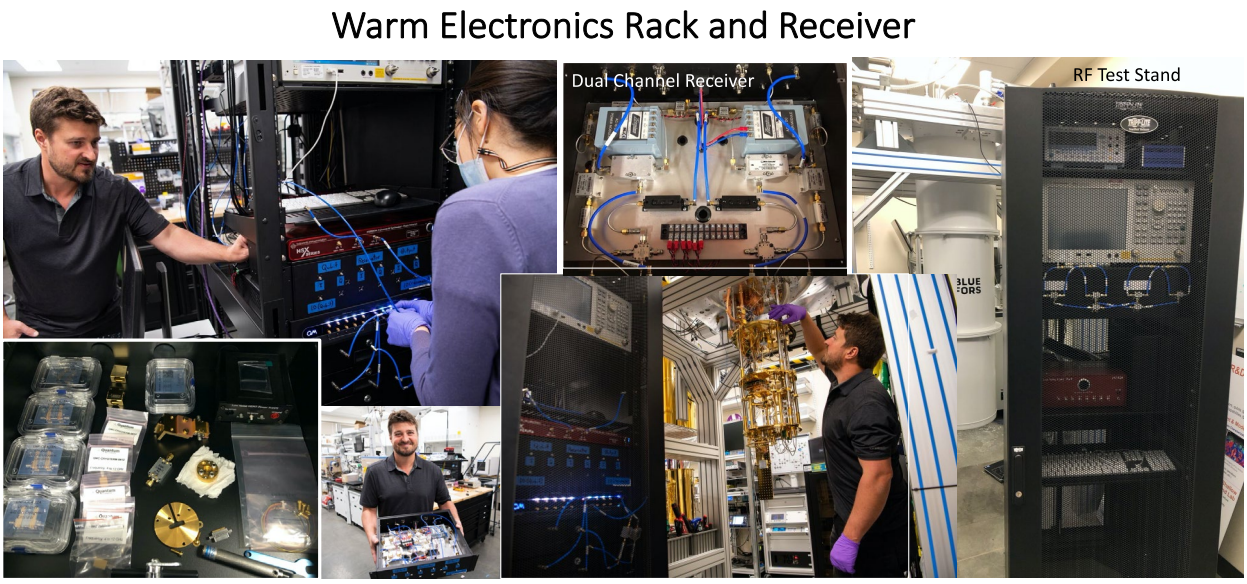

Figure 7. RF test stand rack and dual channel receiver.

3.3.3 Software

Administration of the rack server was accomplished using the ansible automation toolset, using YAML files called playbooks. These playbooks serve the dual purpose of documenting the system configuration and making reconfiguration in the event of operating system (OS) issues trivial. The disks were also configured so that the user's home directories, and a large data shared/archive directory, were on a separate physical disk from the OS. This allows the OS to be safely installed without threatening any user or experiment data, and the ansible playbooks mean that a freshly installed system can be reconfigured to its previous state in minutes, minimizing downtime.

To coordinate the various measurements necessary to characterize devices like the JPA and JPC (collectively referred to as JPX), a software suite to control the warm hardware instruments was developed. We implemented a python module with SCPI (standard commands for programmable instruments), or pseudo-SCPI, interfaces to the VNA, the RF switches, the Holzworth and SignalCore synthesizers, and the current source. A separate python module was also created to control the AlazarTech digitizer. For convenience, we also implemented a web-based dashboard that could perform basic control and diagnostics of these instruments, including visualizing scans from the VNA and digitizer (See Figure 8).

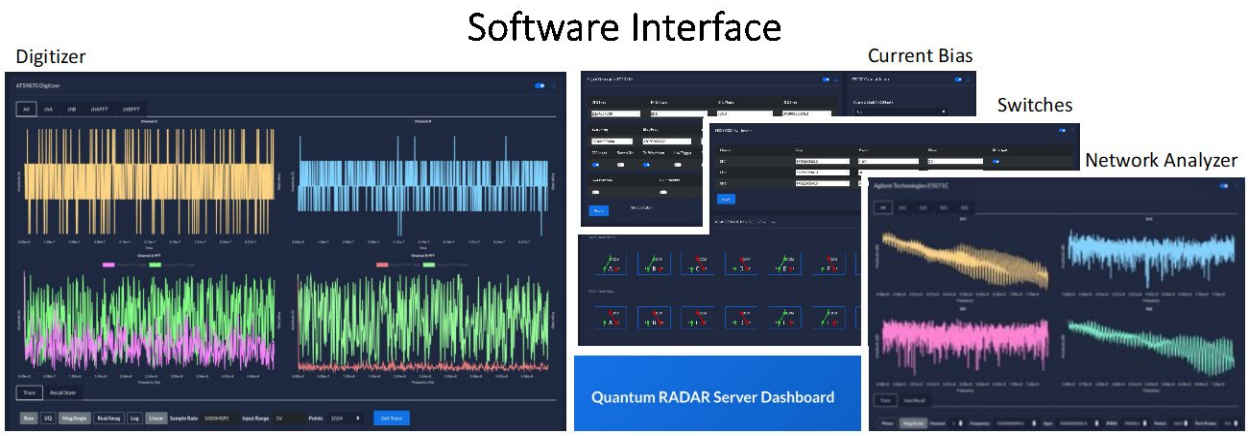

Figure 8. Samples of visualizations from the custom web-based dashboard interface.

The design of the SCPI interface module was compatible with devices that used any text-based commands, even if they were not SCPI compliant, e.g. the Mini-Circuits RF switches. It also made adding additional instrument interfaces and features extremely straightforward: once the set of text commands is determined, a class method is written that formats the command properly based on the given arguments and sends it to the device using a generic backend. This makes adding software support for new instruments trivial.

With these libraries, several sophisticated scripts to characterize the JPX devices were developed. These measurements included: collecting mode maps along the JPX bias currents, automatically detecting mode frequencies, and intelligently tuning pump frequencies to collect gain and conversion measurements. We also created scripts to visualize the data collected during these measurements. The scripts were designed to take their measurement parameters from YAML config files, allowing the script code to remain simple, generic and unchanged between runs.

4.0 Data Runs

This section discusses the 7-8 dilution refrigerator data-runs devoted to testing quantum devices.

4.1 Preliminary JPA runs

As equipment continued to arrive in Q4 of FY21 and Q1 of FY22, preliminary data-runs designed to test contributed JPA devices as well as the supporting electronics were conducted. A schematic of the preliminary test is shown in Figure 9. The testing protocol was:

1. Perform a reflection measurement off the JPA device and measure a phase shift as a function of bias current. This was done by using a VNA to inject a swept signal to the JPA via a circulator in the cold space. The signal is reflected off the JPA, travels back to the circulator, and is then read out by the VNA. The VNA is set to either perform an "unwrapped" phase measurement or a phase measurement for which the cable length has been accounted (to avoid excessive wrapping between -180 and 180 degrees). A resonance produces signature 360 degree phase shift across its envelope, also a 2D power spectrum intensity plot can be used to identify the resonance as a prominence. Measurements can be repeated at different bias currents in order to form maps of the Signal and Idler modes.
2. Operate the JPA as an amplifier by achieving gain. The bias was tuned to a region of steep linear resonance tuning on the mode map. Linear is a requirement to minimize higher order non-linearities. A signal generator was used to pump the JPA at a frequency that was 10-15 MHz away from the center frequency. ON/OFF measurements were performed where a plot of the ratio of the spectrum with the pump on and off where produced for a variety of pump powers.

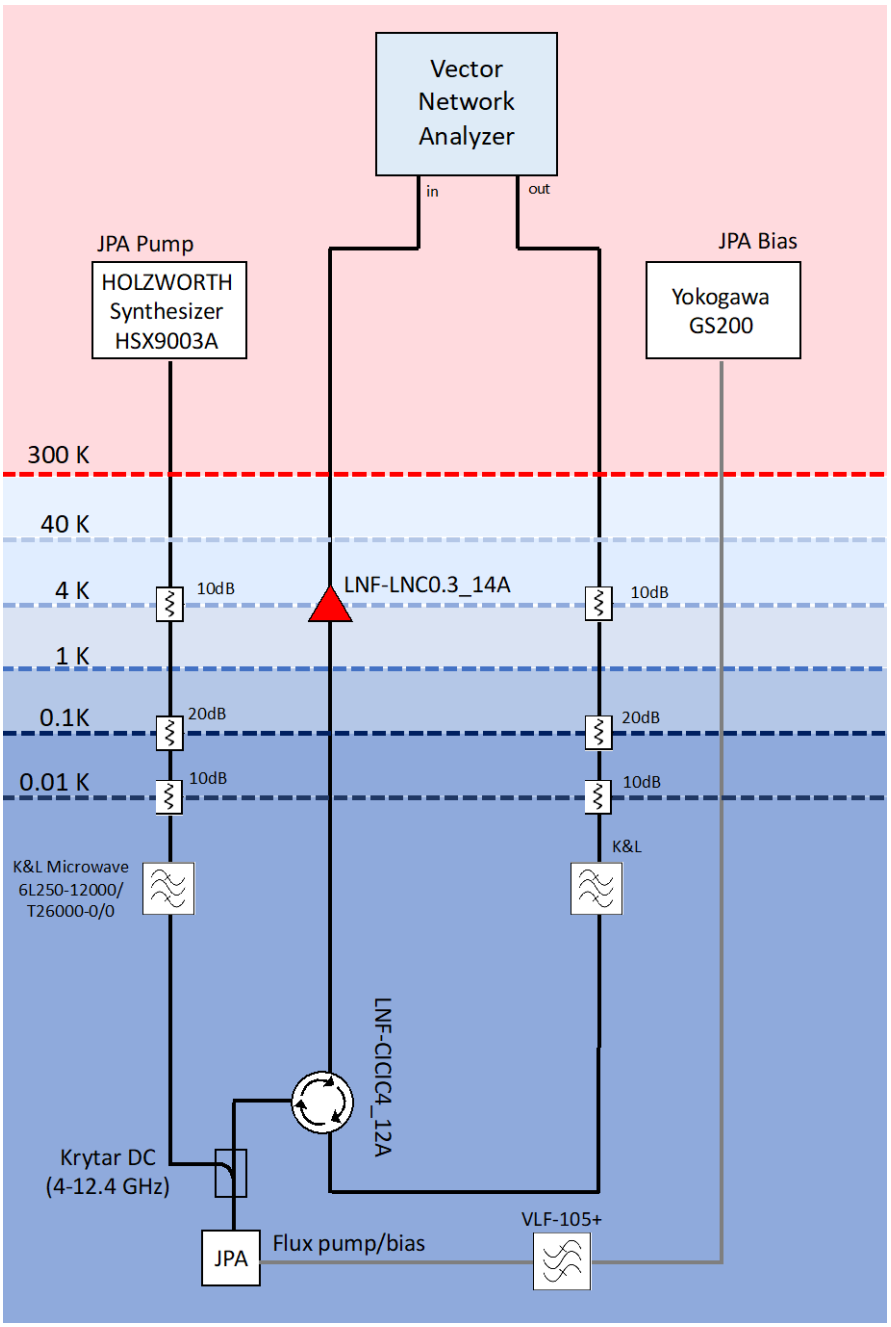

Figure 9. JPA testing schematic.

4.1.1 BBN Raytheon JPA

The first run, performed with the BNN Raytheon JPA, confirmed in-house HEMT amp wiring, HEMT and circulator health, as well as provided practice for fragile RF wiring in the dilution refrigerator. However, no resonant mode or flux tuning was observed. In retrospect, it was discovered that more room temperature amplification was necessary for adequate SNR. Two Mini Circuits ZX60-123LN-S+, each supplying 17 dB of gain were placed directly on the cold space output for future runs.

4.1.2 U. Chicago JPA

On November 19th, 2021 JPA resonance tuning was observed for the first time at PNNL. The 2D contour plot in Figure. 10 shows the phase of a VNA measurement (depicted as a color) as the sequence of vertical slices strung together as a function of bias current. Here, the arc represents the resonant mode of the JPA tuning at its peak of ~6 GHz to (and below) 3.5 GHz, which is out of the circulators' operational range; this is why the map becomes unreadable below 3.25 GHz.

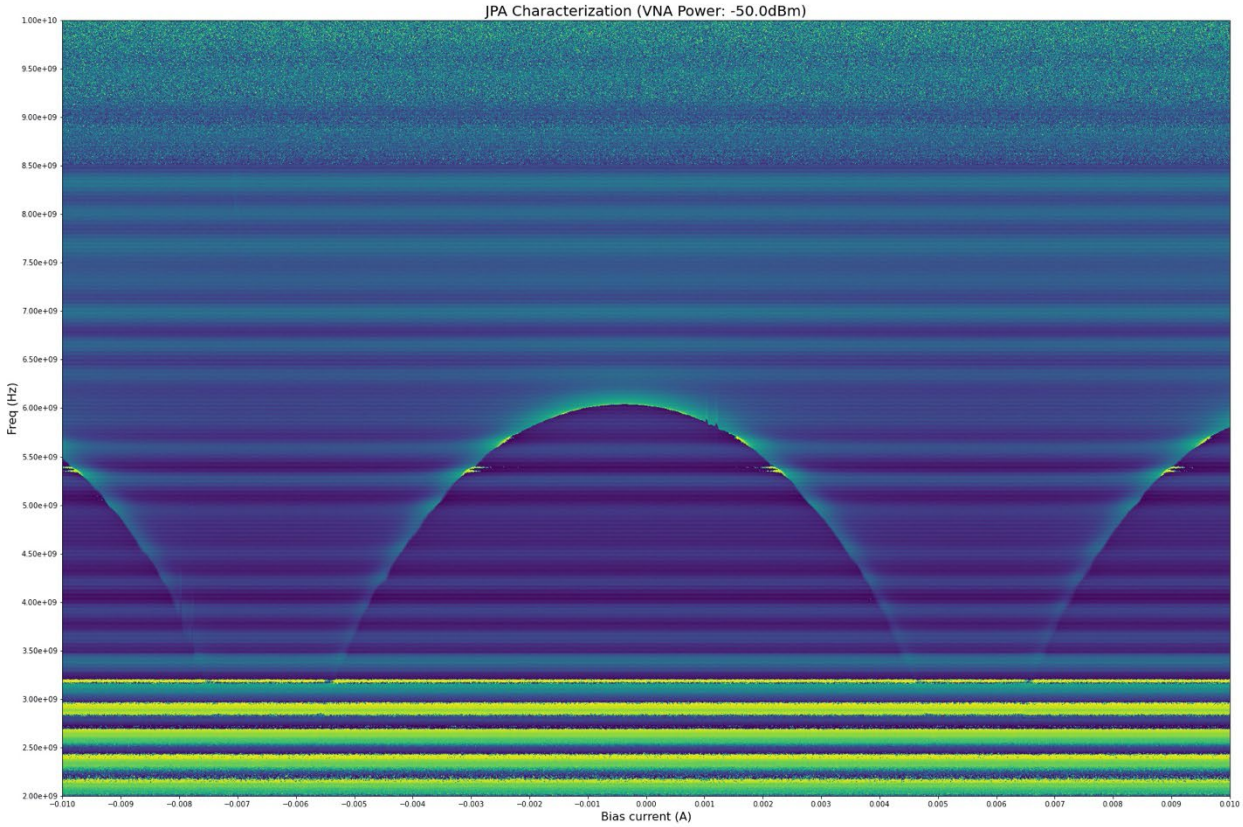

Figure 10. JPA resonance versus bias current

Supplying the JPA with a pump tone and performing ON/OFF measurements did result in gain (exhibiting amplifier behavior) but the measurements were very noisy (see Figure 11). It was determined that within the thermal shields the JPA remained highly susceptible to magnetic and RFI noise. In fact, it was observed, during this data run, that rotating a credit card (containing a magnetic strip) was sufficient to shift the resonant frequency of the JPA four feet away from the dilution refrigerator. These preliminary measurements were performed before the delivery of a magnetic shielding unit, which was expected to reduce magnetic and RFI noise by at least 20dB.

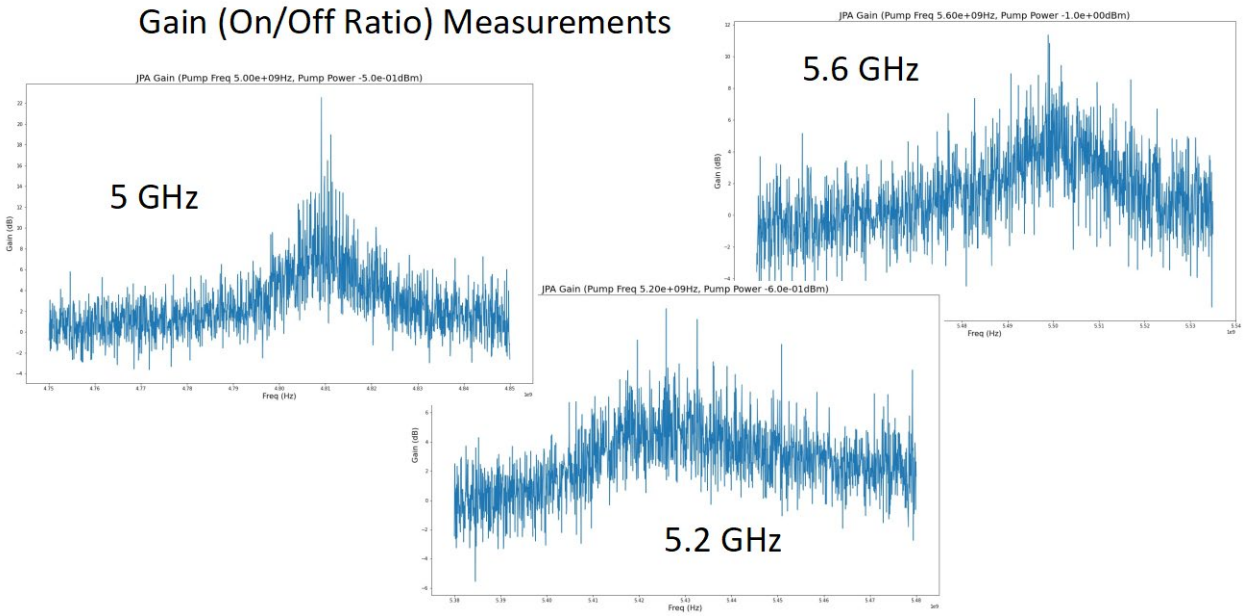

Figure 31. Noisy ON/OFF gain measurements performed before delivery of magnetic shielding.

4.2 JPC Runs

Three Hatridge Lab JPC devices were shared with the LDRD project. JPC measurements began in February of FY22. The testing protocol (similar to the JPA protocol) was as follows:

1. Create a mode-map by performing reflection measurements off the JPC's Signal and Idler channels, measure their phase shifts and power spectra as a function of bias current.

2. Explore a sub-range of biases where the resonances tunes quickly and linearly.

    a. Measure both the Signal and Idler frequencies (f_S and f_I).

    b. Observe gain by pumping the JPC at the sum of the Signal and Idler frequencies ($f_P = f_S + f_I$) and taking the ratio of measurements with the pump On and Off.

    c. Conversion (where the pump converts photons in one channel into photons in the other channel) by pumping the JPC at the difference of the Signal and Idler frequencies ($f_P = f_S - f_I$) and taking the ratio of measurements with the pump On and Off.

    d. Digitize data and observe squeezing. While the JPC is being pumped at the sum of the frequencies, digitize the outputs of the mix-down receiver and look for correlations in Signal and Idler noise in I and Q quadratures.

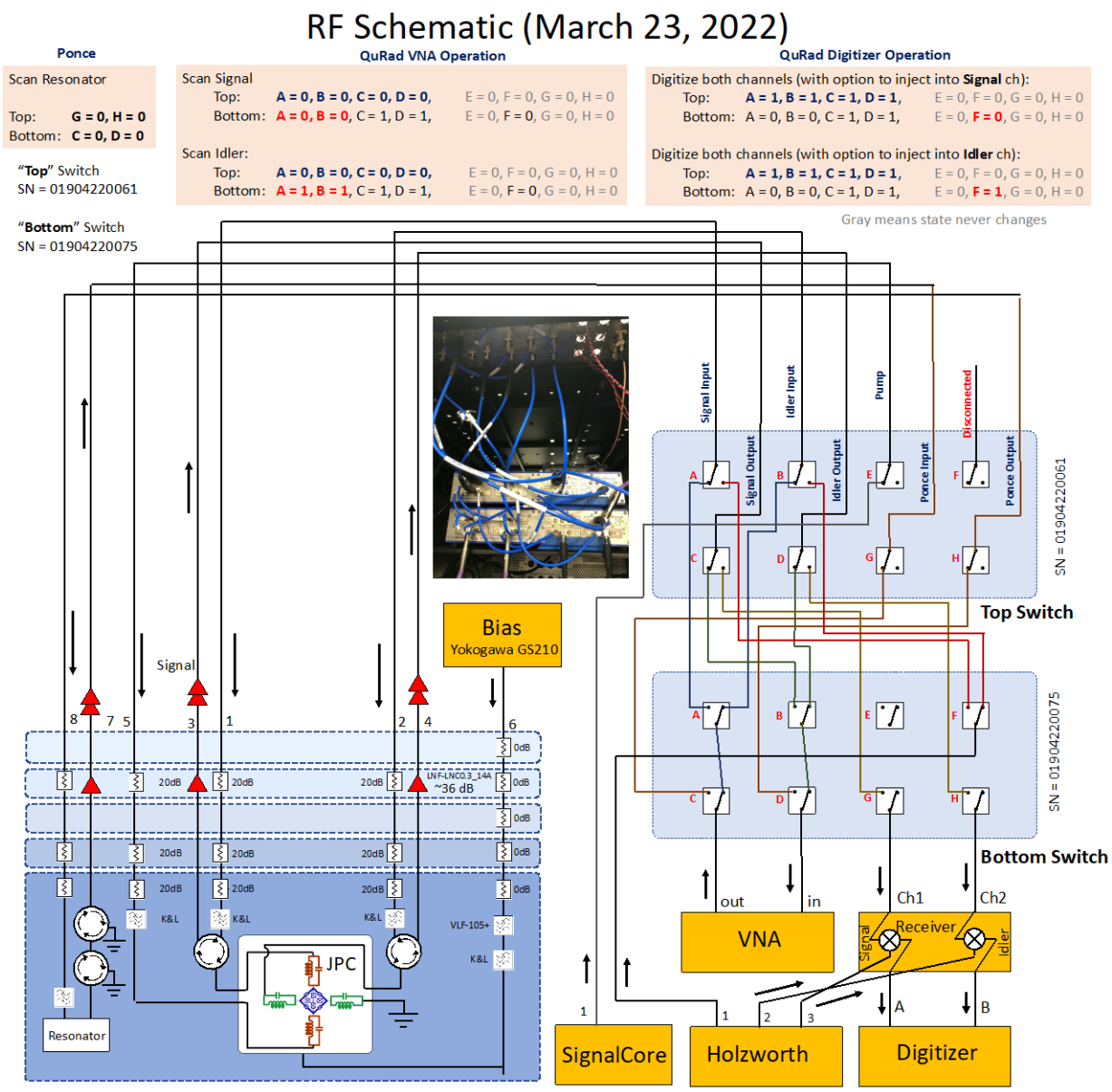

Figure 42. JPC testing RF schematic

4.2.1 JPC 43

The first device to be tested was the Hatridge group's JPC #43 in February of FY22. Figure 13 shows the mode map (resonance of mode phase versus bias current) for the Signal channel. This was also the first mK run that involved using the newly acquired cryoperm magnetic shielding, which gave much cleaner and more stable phase and power spectra.

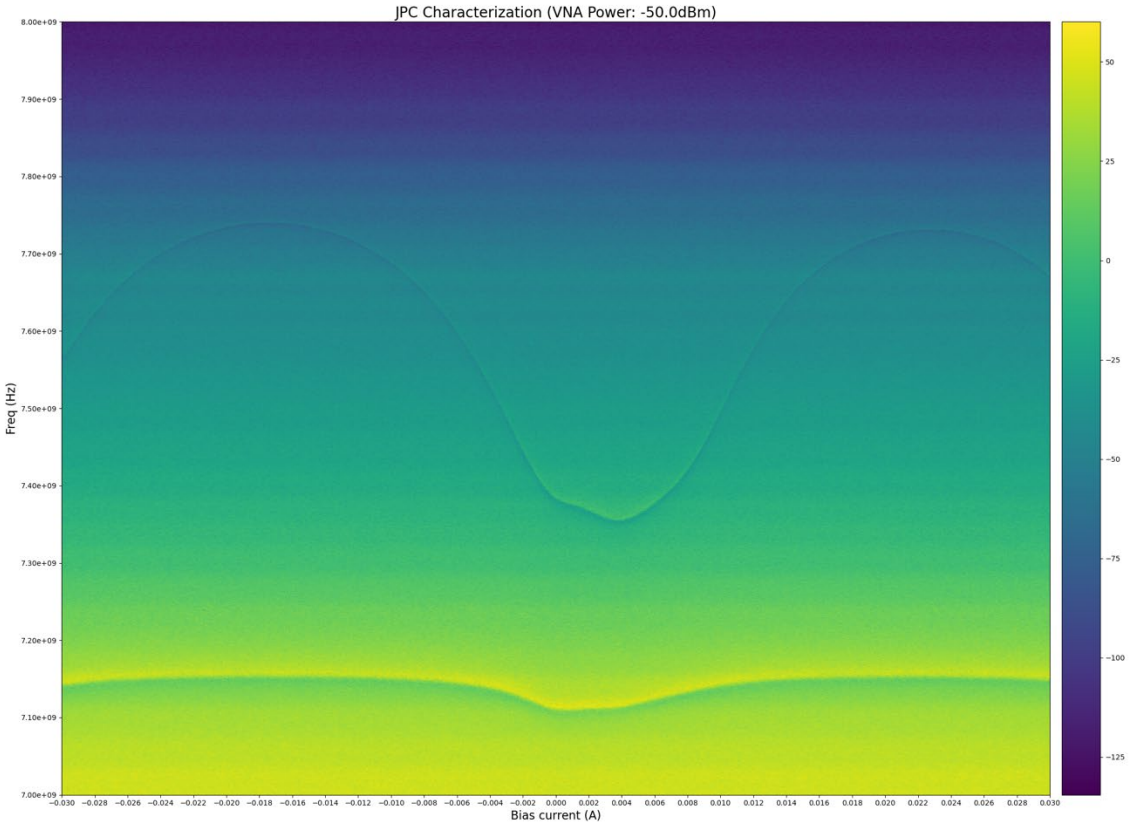

Figure 53. JPC 43 Signal port phase delay mode map. The upper modulating feature was determined to be the Signal resonance feature due to its large tuning range. The lower feature's origin is unknown.

The figure shows the signal mode tuning as a function of bias current. The plot shows an asymmetry around the lowest frequency of the mode and is also missing a double trough characteristic seen in the subsequent devices. It was hypothesized that trapped flux was interfering with JPC behavior.

Additionally, there is no equivalent figure for the Idler channel because, unfortunately, there was no visible tunable mode discovered in testing. Given the non-functioning Idler channel and the asymmetric Signal channel, the decision was made to warm up.

4.2.2 Repairing broken ("rattling") JPCs

Upon inspection of JPC 43, it was discovered that it rattled slightly when the case was gently shaken. This discovery prompted an examination of the other JPCs and JPC 44 was also found to rattle. Disassembly of the rattling JPCs revealed that the chip had become unglued from its mount, see Figure 14. It is unknown for either JPC 43 or 44 if their chip became unfixed during storage, shipment to PNNL, or handling and installation in the lab. Both had their chips GE varnished back down to the enclosure back-plane and had their severed connections re-connected with wire bonds.

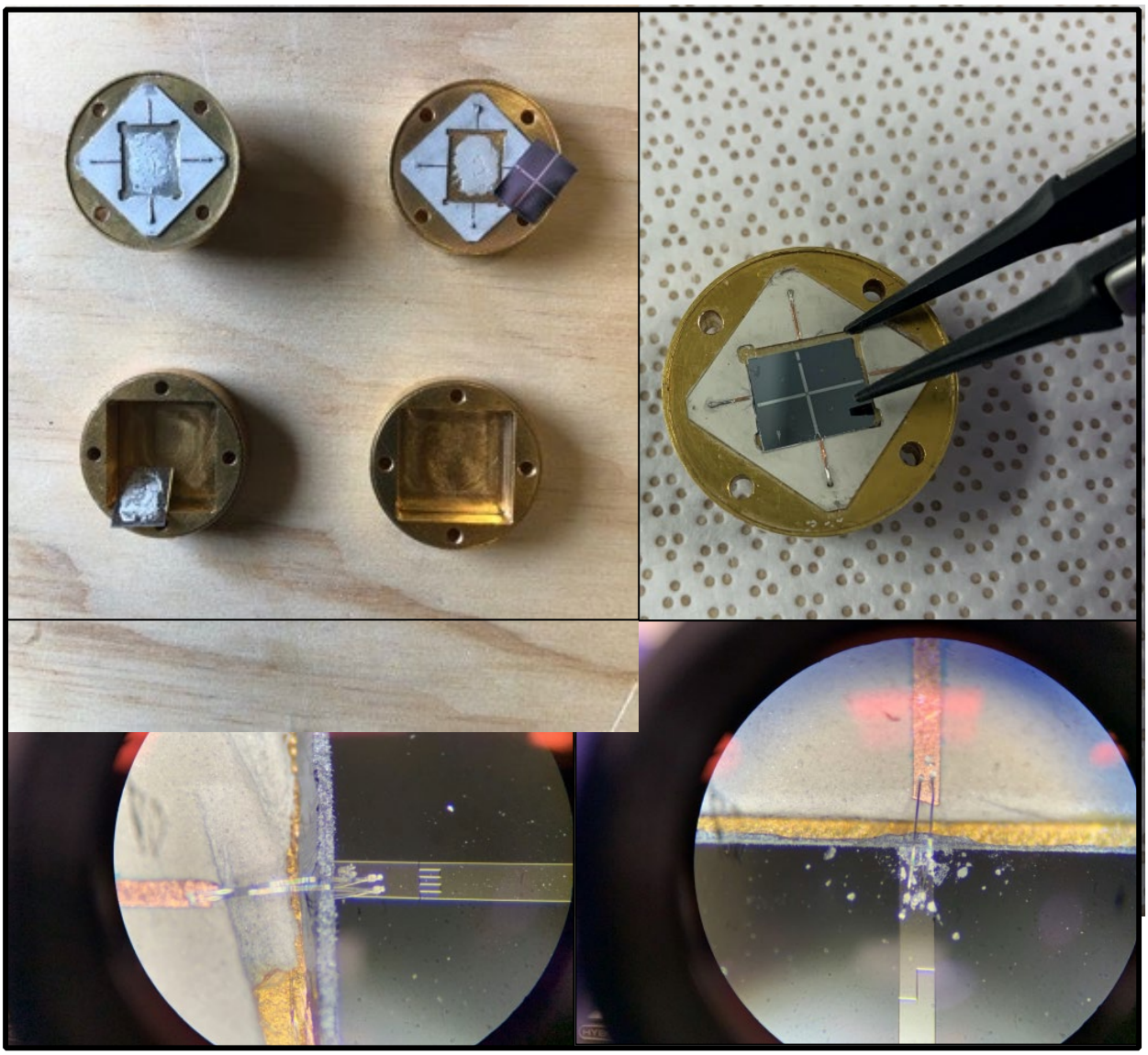

Figure 64. JPC repair. (Upper left) JPCs 43 and 44 with cases open, showing chips that are partially or completely unfastened. (Upper right) JPC chip being repositioned on its mount. (Lower) Examples of wire bonds between Cu leads and the Ni

4.2.3 JPC 42

While JPC 43 and 44 were undergoing repairs, JPC 42 was installed in the dilution refrigerator. Figure 15 shows the phase delay over bias current and frequency for both working Signal and Idler channels. Here, color indicates phase.

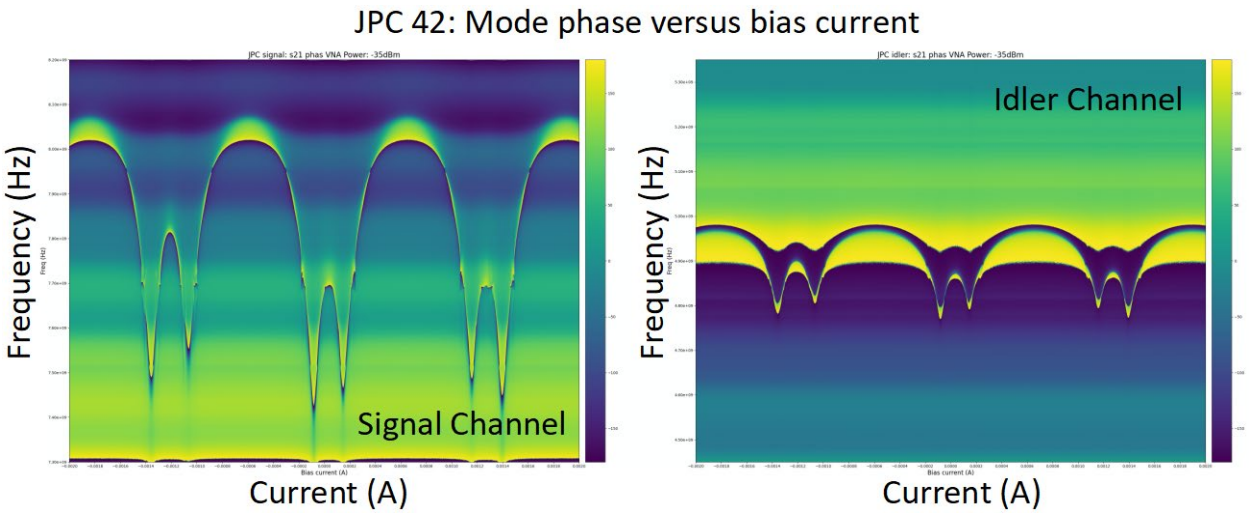

Figure 75. JPC 42 mode maps for Signal and Idler channels.

In order to achieve gain in both channels, a range of current biases was chosen to correspond with mode map regions where the slope of the mode is steep and linear. Figure 16 illustrates our three step process for configuring the device for amplification:

3. A bias is picked for which both Signal and Idler modes exhibit linear behavior. An example of such a bias is marked by the vertical red line,
4. For a given bias, measure both the Signal and Idler mode frequencies,
5. Set the pump frequency equal to the sum of the Signal and Idler frequencies.

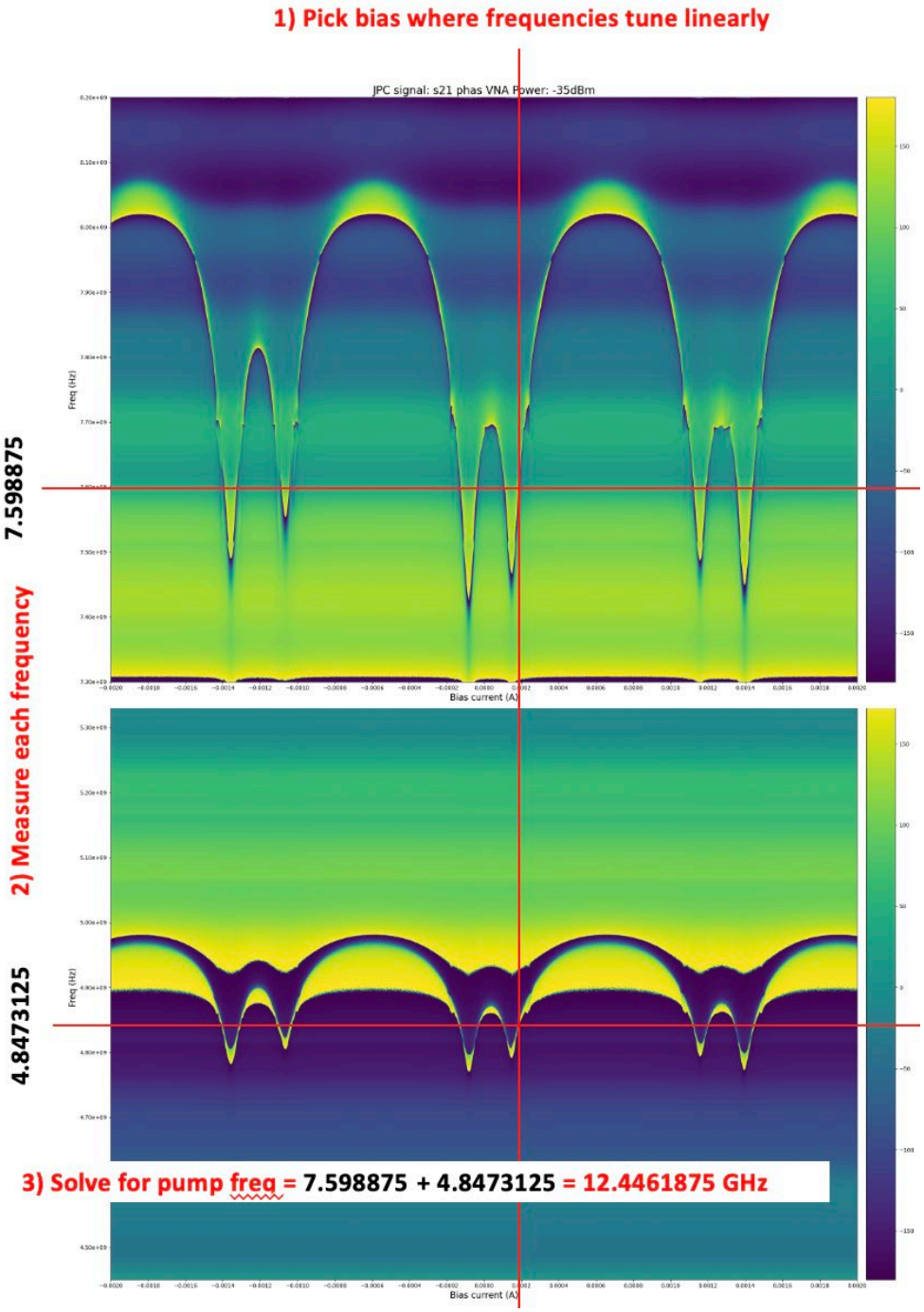

Figure 86. Illustration of 3-step process for achieving amplification in both channels.

Setting both channels of the JPC up for amplification reliably, over the course of many different data runs and circumstances, required being able to follow and measure both mode frequencies in an automated way. A mode-tracking routine that used combined information from both the minimum of the log magnitude power measurement and derivative of the phase was written for efficient device characterization. Figure 17 shows the routine using both magnitude power (left) and phase (right) information to pick out the resonant mode (red).

Mode Tracking

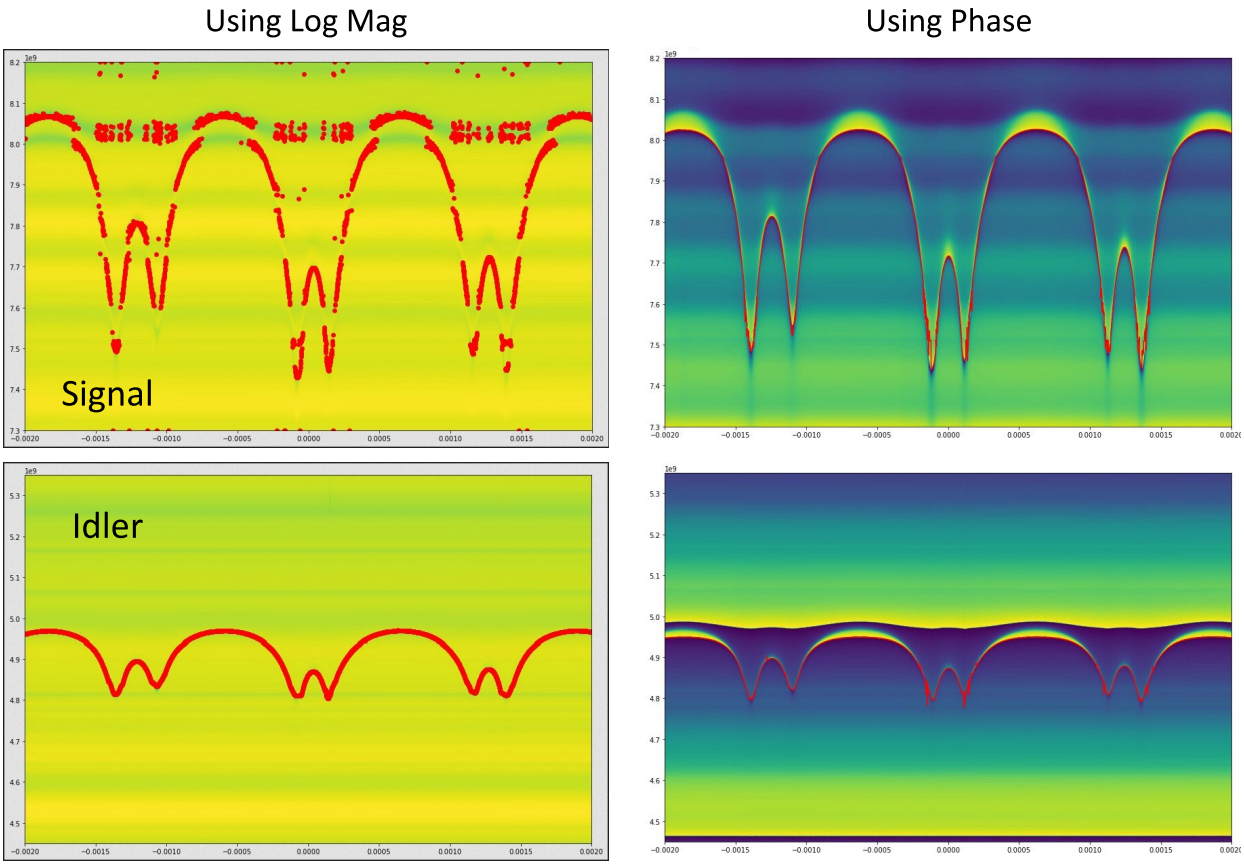

Figure 97. An early version of the mode tracking routine identifying resonant mode using both magnitude (left) and phase (right) information, as applied to JPC 42.

Building on procedures and techniques discussed, gain measurements of both Signal and Idler channels were performed for a ranged of current biases (Fig. 17). For each figure, each VNA S12 trace represents the ratio of pump ON and pump OFF measurements where colors indicate an iteration through a range of pump powers.

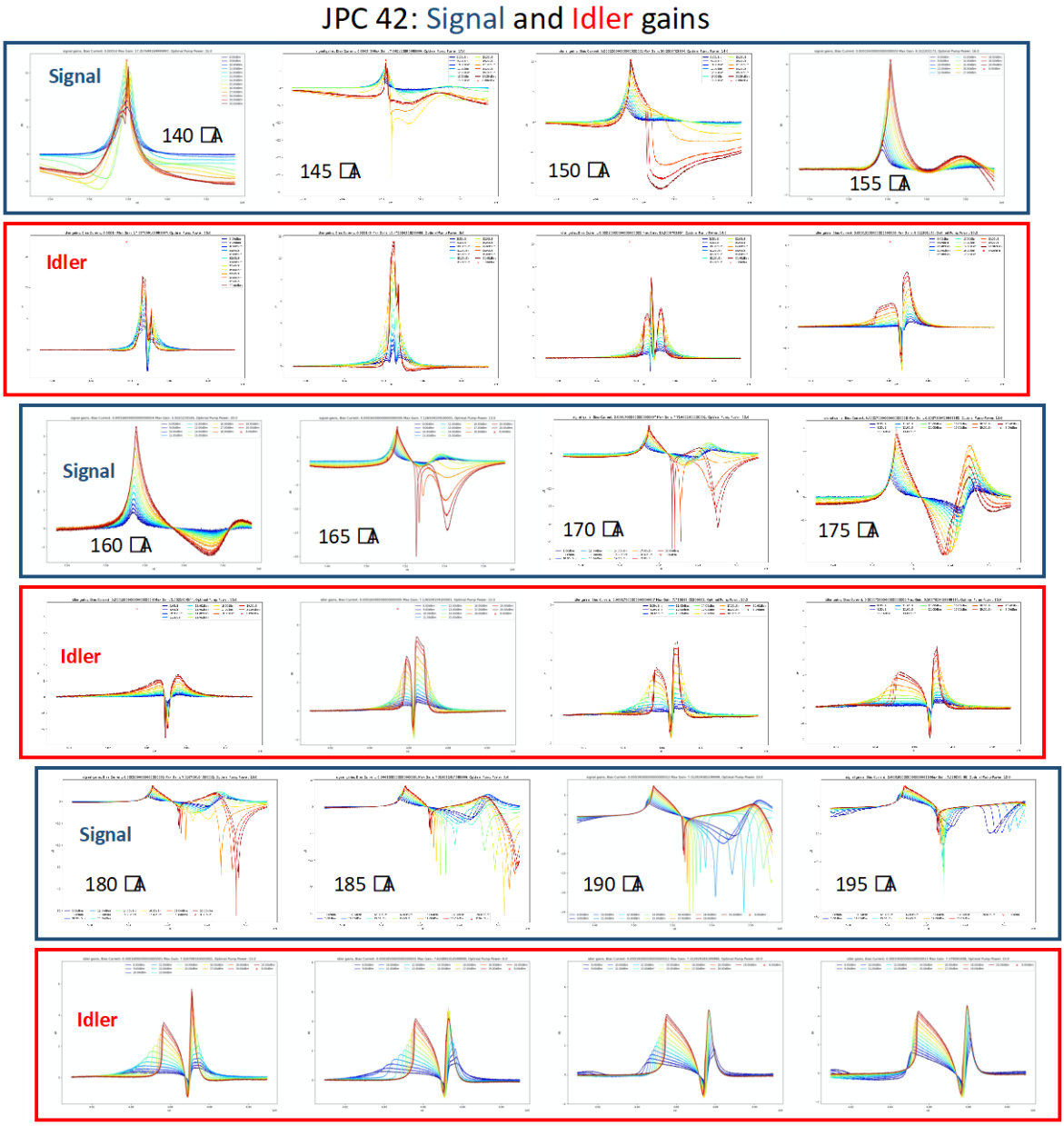

Figure 108. Examples of gain curves for JPC 42 over select current biases and pump powers. Individual plot panels are for a fixed current bias and channel, with rows outlined in blue indicating the Signal channel and rows outlined in Red indicating the Idler channel.

The anticipated spectral shape for gain resonance is a well-behaved Lorentzian peaking at 10 - 25 dB. Figure 18 is a good example of what was observed over the course of many different runs using different devices. In some cases, trapped flux in the JPC was suspected. In these cases, the fridge was warmed to 4K and cooled back down again. In other cases, it was believed that the perhaps the mode structure had shifted and mode mapping was performed again. Measurments were not repeatable and the external collaborators who manufactured the JPCs were unable to explain these results.

Figure 19 shows a series of plots used for debugging the digitizer analysis code developed on this project. For this exercise, a tone was injected into the receiver and the time-series

digitization was plotted (left). The time series was then histogram (center) and then Fourier decomposed into the IQ plane (right).

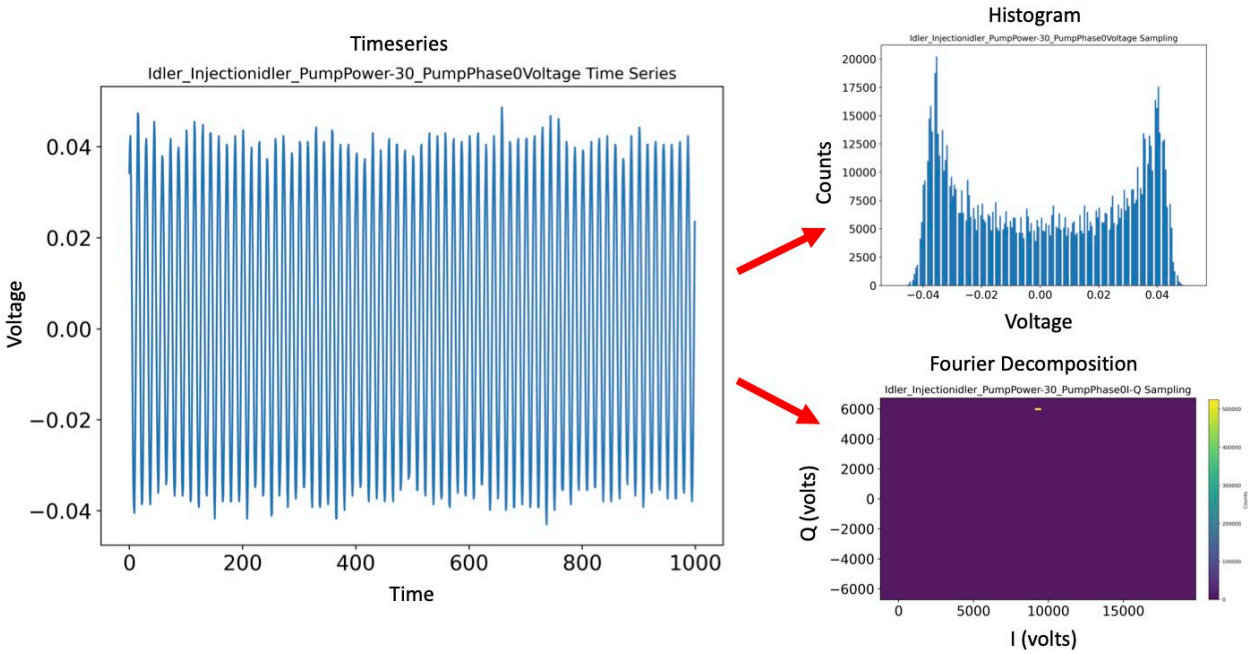

Figure 119. Digitization of a tone injected into the receiver. A raw voltage timeseries (left), a histogram of the timeseries (right, upper), and an I-Q decomposition of the time series' power spectrum (right, lower) is shown. The I-Q plot clearly shows the injected tone as an offset of the distribution centroid from the origin. The injected tone reshapes the time series histogram from the more normal distribution of pure thermal noise to the bi-modal distribution dominated by the endpoints of the injected tone's sinusoid waveform.

Had normal amplifier behavior been observed, the next planned procedural step was to digitize output from the Signal and Idler ports and demonstrate entanglement of photons between channels. In this scenario, signals mixed down to 70 MHz in the receiver would be time-wise digitized and Fourier decomposed into IQ quadratures. Squeezing of the thermal excitations in the JRM would appear as an IQ plane anisotropy (elliptical in shape) of the normal modes' excitation distribution, which in an unsqueezed state would appear as a, isotropic (circular symmetric) normal distribution. Note that the individual Signal and Idler IQ decomposition would not individually show this squeezing; one must superpose into the normal mode basis to see the correlation. The angle and degree of the squeezing anisotropy are dependent on the squeezing factor (a function of pump power and mode losses) and the pump phase angle relative to the phase angle of the LOs, which are phase-locked together.

4.2.4 JPC 44

Characterization of the third JPC 44 began in July FY22. Figure 20 shows the mode maps for the Signal and Idler channels, including zoomed-in measurements over the relevant biases.

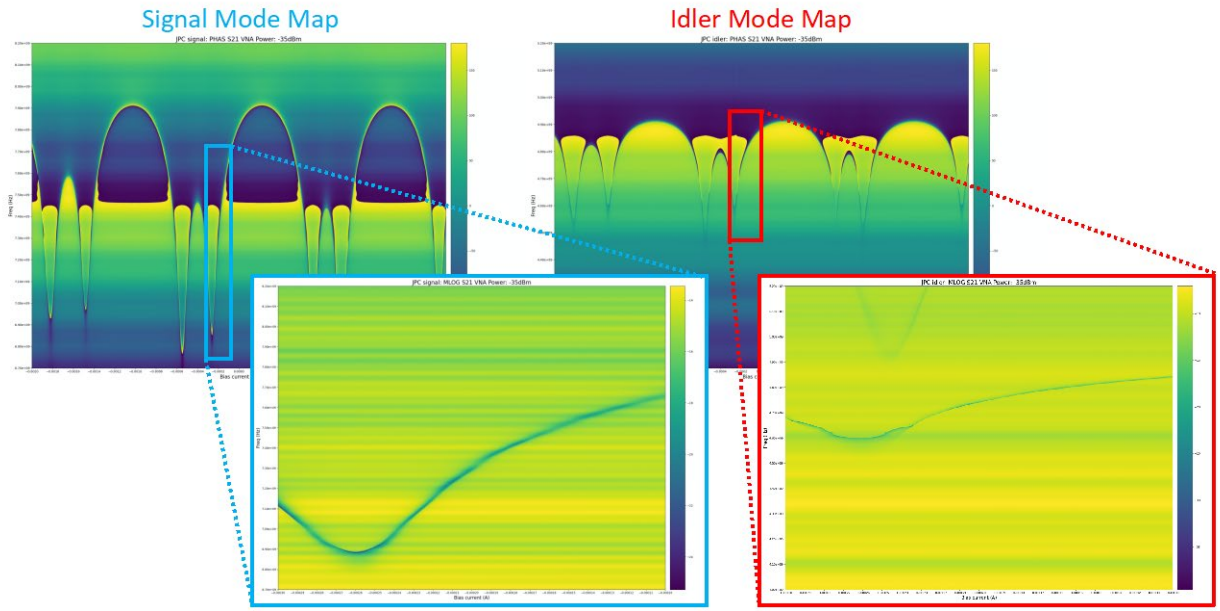

Figure 20. Mode maps of JPC 44. Background images are the phase mode maps of the Signal (left) and Idler (right) channels. Foreground images are zoom-in mode maps of the magnitude power spectra over a subset of current biases. Again, the Signal channel is left and the Idler channel is right.

The automated steps for setting up the device and performing gain measurements (described in the JPC 42 section) were repeated. Figure 21 shows two examples of gain measurements, for Signal and Idler channels, where pump power was varied. It was discovered that the pump power needed to be reduced by 10 - 20 dB compared to previous device measurements to avoid gain saturation. This may have been due to a stronger coupling to the JPC pump port. Unfortunately, the anticipated smooth single peak amplifier behavior was not observed.

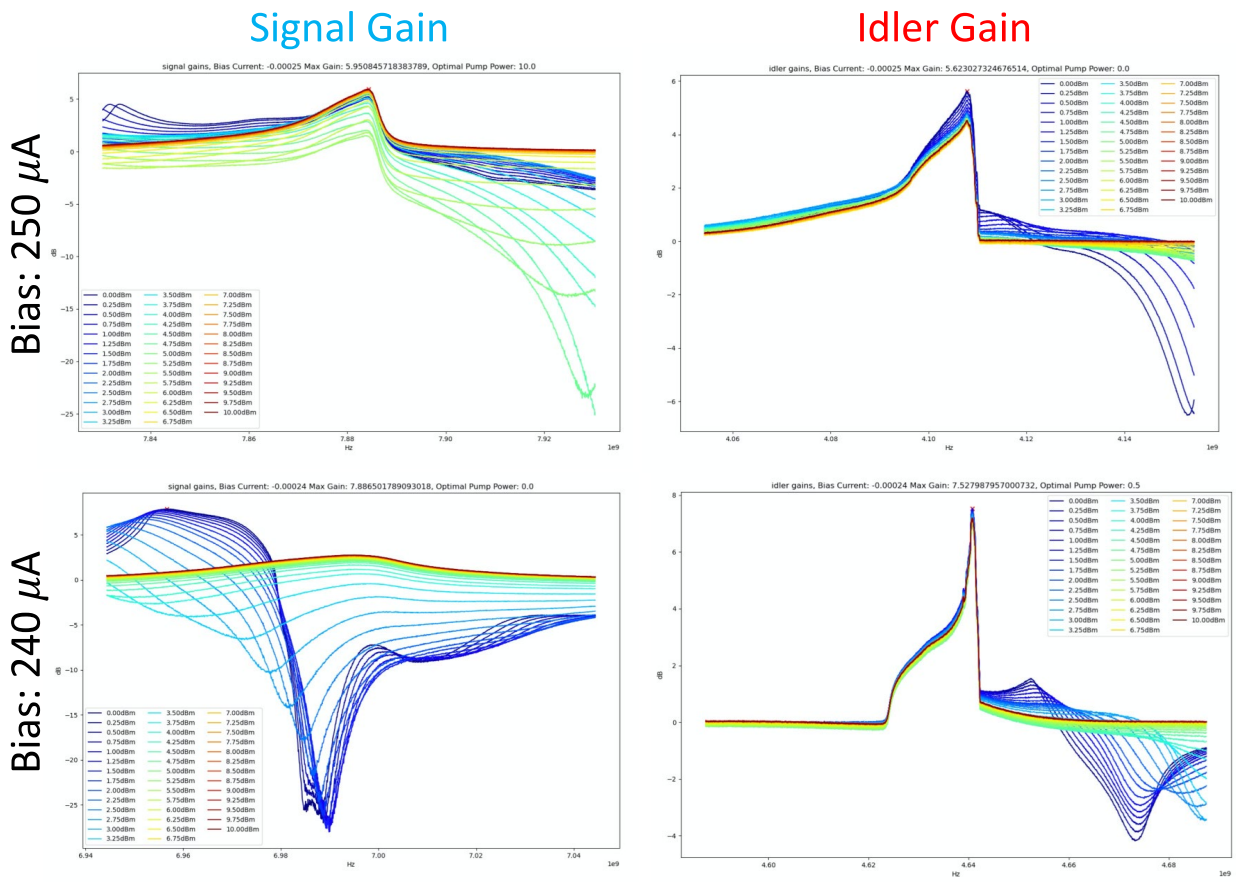

Figure 21. Varied pump power gain curves for Signal and Idler channels featuring two different current biases.

4.2.5 Data Run Closeout

JPA and JPC devices (5 devices total were tested over the course of 7-8 cool-down/warm-up dilution refrigerator data runs. Mode tuning was observed, gain was achieved, and hands-on expertise was acquired. However, JPC measurements did not repeatably match anticipated specs. No squeezing or entanglement was observed which was a prerequisite for demonstrating a quantum radar.

5.0 Conclusion/Summary

In addition to an aggressive schedule that involved first building from scratch a new low temperature RF capability and then second, performing cutting edge quantum radar research in a span of two years, there were also several unforeseen challenges. These challenges included: loss of all key radar staff, broken devices that didn't repeatably meet specifications, procurement delays, and dilution refrigerator scheduling issues. Nonetheless, the project succeeded in meeting its objectives, marked by the three (tools, team, ties) pillars. After two years of procurements, several hundreds of hours software development, custom RF hardware design, repeat R&D testing and debugging, intense networking, and team building, PNNL now has a functioning low temperature RF capability.

Today, this same team at PNNL is characterizing superconducting qubits, microwave Kinetic Inductance Devices (MKIDs), quantum noise limited parametric amplifiers, and SQUIDs for external sponsors and special programs. That R&D heavily leverages the hardware, software, expertise, and community support developed by this strategically timed and scoped LDRD project.

6.0 References

[1] S. Lloyd, Enhanced sensitivity of photodetection via quantum illumination. Science 321, 1463–1465 (2008).

[2] J. H. Shapiro, “The Quantum Illumination Story”, arXiv:1910.12277 (2019)

[3] S. Barzanjeh, S. Pirandola, D. Vitali, J. M. Fink, Microwave quantum illumination using a digital receiver. Sci. Adv. 6, eabb0451 (2020).

[4] D. Luong, C. W. S. Chang, A. M. Vadiraj, A. Damini, C. M. Wilson and B. Balaji, "Receiver Operating Characteristics for a Prototype Quantum Two-Mode Squeezing Radar," in IEEE Transactions on Aerospace and Electronic Systems, vol. 56, no. 3, pp. 2041-2060, June 2020, doi: 10.1109/TAES.2019.2951213.

[5] D. Luong, C. W. S. Chang, A. M. Vadiraj, A. Damini, C. M. Wilson and B. Balaji, "Receiver Operating Characteristics for a Prototype Quantum Two-Mode Squeezing Radar," in IEEE Transactions on Aerospace and Electronic Systems, vol. 56, no. 3, pp. 2041-2060, June 2020, doi: 10.1109/TAES.2019.2951213.

[6] Eichler C, Bozyigit D, Lang C, Baur M, Steffen L, Fink J M, Filipp S and Wallraff A 2011 Observation of two-mode squeezing in the microwave frequency domain Phys. Rev.Lett. 107 113601 (2011).

[7] S. Boutin, D. M. Toyli, A. V. Venkatramani, A. W. Eddins, I. Siddiqi, and A. Blais, Effect of Higher-Order Nonlinearities on Amplification and Squeezing in Josephson Parametric Amplifiers, Phys. Rev. Appl. 8, 054030 (2017).

[8] K. G. Fedorov, F. Deppe, R Gross, A. Marx, M. Partanen, Y Nakamura, K. Inomata, Y. Nojiri, Q. Chen, R. Di Candia, S. Pogorzalek, M. Renger, “Experimental quantum teleportation of propagating microwaves”, Sci. Adv. 7, eabk0891 (2021).

[9] Cao, Xi (2021) Quantum Measurement and Bath Engineering for Superconducting Qubits via Multiple Parametric Couplings. Doctoral Dissertation, University of Pittsburgh.

[10] G. Liu, X. Cao, T. -C. Chien, C. Zhou, P. Lu, and M. Hatridge, “Noise reduction in qubit readout with a two-mode squeezed interferometer”, arXiv:2007.15460 (2020).

Pacific Northwest National Laboratory

902 Battelle Boulevard
P.O. Box 999
Richland, WA 99354

1-888-375-PNNL (7665)

www.pnnl.gov